Characterisation of deuterium distributions in corroded zirconium alloys using high-resolution SIMS imaging

Junliang Liu[1], Kexue Li[1,2,*], James Sayers[1], Thomas Aarholt[1,3], Guanze He[1], Helen Hulme[2,4], Alistair Garner[2], Michael Preuss[2], Heidi Nordin[5], Jonna M. Partezana[6], Magnus Limbäck[6], Sergio Lozano-Perez[1], Susan Ortner[7], Chris R.M. Grovenor[1]

[1]Department of Materials, University of Oxford, Parks Road, OX1 3PH, Oxford, UK.
[2]Department of Materials, University of Manchester, Oxford Road, Manchester, M13 9PL, UK.
[3]Department of Physics, University of Oslo, Oslo 0316, Norway.
[4]Jacobs, Walton House, Birchwood, WA3 6GA, UK.
[5]Canadian Nuclear Laboratories, Chalk River, ON K0J 1J0, Canada.
[6]Westinghouse Electric Sweden AB, SE-721 63 Västerås, Sweden.
[7]National Nuclear Laboratory, Culham Science Centre, Abingdon, Oxon, OX14 3DB, UK.

[*]Corresponding author: E-mail address: kexue.li@manchester.ac.uk (Kexue Li)

Abstract

Hydrogen diffusion through the oxide grown on Zr alloys by aqueous corrosion processes plays a critical role in determining the rate of hydrogen pickup (HPU) which can result in embrittlement of fuel cladding and limit the burnup of the nuclear fuel it encapsulates. Mapping the hydrogen/deuterium distributions in these oxide layers, especially in the barrier layer close to the metal/oxide interface, is a powerful way to understand the mechanism of both oxidation and hydrogen pickup. Here we have characterised by high-resolution SIMS analysis the deuterium distribution in oxide layers on a series of Zr alloys, including autoclave-oxidised Zircaloy-4, Zr-1Nb and Zr-2.5Nb alloys, and in-flux and out-of-flux corroded Zr-2.5Nb samples. Pre-transition Zircaloy-4 samples show a high deuterium trapping ratio in the oxide and a higher diffusion coefficient than in oxides on the Nb-containing samples. Neutron irradiation increases the deuterium diffusion coefficient, the deuterium concentration in the oxide and the pickup fraction in Zr-2.5 Nb samples. Comparative NanoSIMS and EDX/SEM analysis demonstrates that the deuterium is not preferentially trapped at second phase particles in the oxides on any of the alloys studied, but there is direct evidence for trapping at the surfaces of small oxide cracks especially in Zircaloy-4 samples. The high resolution mapping of these hot-spots in 3D can provide unique information on the mechanisms of hydrogen uptake, and suggests that the development of interconnected porosity in the oxide may be the critical rate-determining mechanism that controls HPU in the aqueous corrosion of zirconium alloys in water-cooled reactors.

Keywords: Zirconium alloys; Corrosion; Hydrogen diffusion; NanoSIMS;

1. Introduction

For many years zirconium alloys have been used as fuel cladding materials in the nuclear industry due to their low neutron capture cross-section, acceptable mechanical properties and adequate corrosion resistance in contact with high-temperature water. However, hydrogen pickup (HPU) during the corrosion of these Zr alloys is still a major limiting factor for achieving high fuel burnup. Water dissociation by both the cathodic reaction and radiolysis results in the creation of free hydrogen that can either recombine to form hydrogen gas released to the cooling water or diffuses through the oxide layer into the Zr matrix and contributes to HPU [1]. If the hydrogen concentration exceeds the bulk solubility, hydrides are formed in the metal during cooling cycles, resulting in a serious reduction in cladding strength [2].

Despite considerable research efforts, the mechanisms by which this hydrogen migrates through oxide layers formed by aqueous corrosion are not well understood. It is reported that the combination of an oxygen vacancy and a hydrogen atom (V_{OH}) is the most stable form of hydrogen in ZrO_2, and can promote hydrogen transport via solid-state diffusion [3, 4]. Previous reports also suggest that hydrogen diffuses through the oxide as protons [5, 6], and Sato et al. [7] have demonstrated a proton migration mechanism on the surface of ZrO_2 in contact with water involving water molecules as proton acceptors and donors. In both mechanisms, proton migration needs to overcome a significant energy barrier and also requires a high concentration of oxygen vacancies since the solubility of hydrogen in stoichiometric ZrO_2 is extremely low [8]. Cox and Wong [6] pointed out that the likely path of hydrogen pickup was via 'structural flaws' in the oxide film, and mechanisms involving the hopping of H^+ between –OH groups or the migration of –OH groups along grain boundaries or through cracks are possible diffusion mechanisms [9]. However, defining a specific mechanism is difficult due to the lack of direct observations on hydrogen distributions and preferred transport paths in the oxide, partly because of the small number of experimental techniques that can be used to analyse hydrogen distributions with high spatial resolution.

Secondary Ion Mass Spectrometry (SIMS) is one of the few techniques that can offer this capability and has been used by several groups to study corroded zirconium alloys [10]. The inner, protective region of the oxide is reported to have high electrical resistance, to be impermeable by the electrolyte and to contain almost no trapped hydrogen [11, 12]. Direct measurements of hydrogen distributions in oxide layers [13] have led to suggestions that compressive stresses generated by the volume expansion when the oxide is formed suppress the diffusion of hydrogen in this protective layer near the metal/oxide interface [14]. There have also been several suggestions for the critical pathways for hydrogen penetration through the oxide based on SIMS analysis. Second Phase Particles (SPPs) have been proposed as preferential diffusion pathways [15-17], although the interparticle spacing is usually not small enough to offer a continuous permeation path. Cracks and pores [6], interconnected porosity [18, 19] and oxide grain boundaries [20, 21] have all been suggested as preferential pathways for hydrogenic, as well as oxidising, species to reach the metal surface. Recent studies have shown that the oxide film has a complicated microstructure containing several different types of nano-porosity [22, 23], and in addition to the bulk ZrO_2 oxide (mostly monoclinic and some tetragonal [24]), a metastable ZrO suboxide may form at the metal-oxide interface [25-28]. Thus there may be several possible pathways for hydrogen ingress, and different specific nanostructures through which the hydrogenic species must pass to reach the underlying Zr metal. It is also interesting to note that the electrical conductivity of the oxide layer has a negative correlation to the HPU fraction (HPUF) in both modelling [29] and Electrochemical Impedance Spectroscopy (EIS) results [30] because a ready supply of electrons reduces the requirement for proton transfer to complete the electrochemical circuit during corrosion. Thus the dominant influence on HPUF depends on the environmental conditions and the stage of the oxidation process, and despite previous experimental and modelling studies the key processes are not yet clearly identified.

In this paper, we focus on the high-resolution SIMS analysis of hydrogen distributions in oxide layers formed on corroded Zr alloys to overcome the experimental problems associated with mapping hydrogen isotopes in thin polycrystalline oxide scales with a high enough spatial resolution to identify diffusion paths. Atom probe tomography (APT) allows the analysis of trace element distributions at nanoscale spatial resolution and with a higher sensitivity than can be achieved by Transmission Electron Microscopy (TEM) analysis [31, 32], but it is limited by complicated sample preparation, and the relatively low mass resolution [33, 34] can also make it challenging to resolve interferences between different hydrogen-containing molecular ions. SIMS has been used to characterise elemental distributions in a wide variety of samples [35-38], and combines excellent depth resolution with high sensitivity for light elements and so is a powerful technique for mapping the interaction of hydrogenic species with the oxide layers formed on zirconium alloys. We have already shown that high-resolution SIMS analysis of oxidised zirconium alloys using a CAMECA NanoSIMS 50 instrument enables the mapping of hydrogen distributions at a sub-micrometre scale with no elaborate sample preparation [12]. However, the interpretation of hydrogen distributions in NanoSIMS analysis is challenging because the signal can originate from hydrogen both from the vacuum system and from surface contamination. More recently, we have demonstrated using deuterium spiking as a surrogate for hydrogen that an analytical methodology can be designed that gives reliable data on the location of deuterium in three dimensions, and allows us to study the critical mechanisms of hydrogen penetration through thin oxide layers formed on zirconium alloys [39]. Here we report the application of this experimental methodology to compare the characteristic deuterium distributions in oxides formed on zirconium alloys with different starting microstructures and trace alloying additions, corroded in different water chemistries, and also to study samples corroded in-reactor that will more precisely mimic the conditions experienced by the fuel cladding tubes in service. We will show that these parameters can strongly influence the details of the pathways for deuterium penetration through the oxide layers at different stages of the oxidation process, and hence how alloy microstructure and chemistry can control the critical transport mechanisms controlling HPU.

2. Materials and Methods

2.1. Sample Description

Three types of Zr alloys with different starting microstructures were provided by the Westinghouse Electric Company and by Canadian Nuclear Laboratories (CNL); recrystallised Zircaloy-4, annealed Zr-1Nb and stress-relieved Zr-2.5Nb. As a result of the different thermo-mechanical treatments involved in the fabrication processes of the Westinghouse and CNL alloys, different grain morphologies and distributions of second phases were developed in these materials. The Westinghouse recrystallised Zircaloy-4 had a final recrystallisation step at 560°C which leads to equiaxed α-Zr grains with small second phase particles homogeneously distributed inside the grains, Figure 1 (a). After recrystallisation, the Zr-1Nb material was held at 720°C for 24 hours resulting in larger second phase particles, but these were Nb-enriched β-Zr (~20 at% Nb) rather than the small β-Nb (~80 at% Nb) precipitates found in the recrystallised alloy, Figure 1 (b). The CNL Zr-2.5Nb alloys were extruded at 815°C and then stress-relieved at 400°C for 24 hours. The microstructures of both matrix and second phases are strongly influenced by the extrusion process so that these Zr-2.5Nb alloys show α-Zr grains elongated in both transverse and longitudinal directions with thin layers of partly decomposed β-Zr lying between the α-Zr grains, Figure 1 (c).

All samples have been exposed to deuterated water for at least part of the corrosion period, and so contain a significant concentration of deuterium that can be mapped with confidence in 3D using the

protocols developed previously [39]. The sample alloys and oxidation conditions are shown in Table 1. Z4-1, Z4-2 and 1Nb-1 were oxidised in an autoclave under the conditions described in Table 1 before being transferred to an autoclave containing pure D_2O for 31 days. Two Zr-2.5Nb samples (2.5Nb-1 and 2.5Nb-2) were exposed in an autoclave filled with D_2O (LiOH, $pH_{25°C}$ =10.5) for 150 and 700 days respectively. Z4-pH-1 and Z4-pH-2 were Zircaloy-4 samples provided by Westinghouse as corrosion coupons exposed in a static autoclave by Jacobs. to 50% D_2O containing two wt ppm Li, 95 wt ppm wt. K and 1050 wt ppm B at 350 °C ($pH_{350°C} \approx 8.8$) for 61 and 147 days respectively [40]. Zr-2.5Nb samples 2.5Nb-3 and 2.5Nb-4 are described as 'in-flux' and 'out-of-flux', respectively. 'In-flux' means that the sample was exposed to neutron irradiation in the Halden test reactor and the 'out-of-flux' sample was corroded in the same water chemistry but without exposure to the neutron flux. Dissolved deuterium (5–7 Nml/kg D_2O) was added to the water chemistry to suppress radiolysis. More details about the water chemistry of Zr-2.5Nb in-flux and out-of-flux tests can be found Table S1 in the supplementary information. The deuterium concentrations in the metal matrices after the corrosion processes were measured for samples 2.5Nb-1~4, and are also listed in Table 1.

Figure 2 shows the weight gain and deuterium concentration measurements for samples 2.5Nb-1~4 on the full sets of samples from which we have selected our specimens. Z4-1 and Z4-2 have, after the second corrosion step in D_2O, are halfway to and close to the first transition in oxide growth kinetics [29]. The 1Nb-1 sample has a similar 2-stage corrosion history and is at a similar stage on the weight gain curve to Z4-1. The two Zircaloy-4 samples corroded throughout in D-spiked water (Z4-pH-1 and Z4-pH-2) are respectively halfway to and after the first transition, but in the water of a higher pH. The two Zr-2.5Nb samples exposed to a water chemistry characteristic of the CANDU reactors with pH 10.5 are well before (2.5Nb-1) and after the transition point (2.5Nb-2). A rather restricted number of in-flux samples was available, and so we have concentrated on the 2.5Nb-3 and 2.5Nb-4 samples (in and out of flux at 325ºC), both with an oxide thickness of ~2.5 µm which for out of flux sample 2.5Nb-4 should place it near the first transition [41]. The vertical grey lines in Figure 2 mark the approximate positions of the first kinetic transition points for each set of alloys corroded under different conditions.

For NanoSIMS analysis, bulk samples of size 7 × 7 mm^2 were cut from the materials corroded in autoclaves using a slow speed diamond saw. An FEI Helios Nanolab 600i at Materials Research Facility (MRF) at the Culham Center for Fusion Energy (CCFE) was used to extract smaller samples from the radioactive materials (2.5Nb-3 and 2.5Nb-4). A step-by-step protocol for the preparation of these small, low activity samples is given in [42]. Before insertion into the NanoSIMS, all samples were coated with 5 nm of platinum to avoid charging from the insulating oxide layer.

2.2. NanoSIMS analysis

SIMS measurements were performed with a Cameca NanoSIMS 50 ion probe instrument. This type of double-focusing secondary ion mass spectrometer is characterised by a high lateral resolution, down to 50 nm for the Cs^+ primary ion source. Primary ions are accelerated by a potential of +8 kV in the Cs source, and the sample is held at - 8 kV, thus giving primary beam energy of 16 keV. Before hitting the sample surface, the primary beam diameter is defined by an aperture (D1) of variable size, and is then focused by an immersion lens to its final spot size on the sample surface. The 300 µm D1 aperture (D1-2) is selected for almost all the analyses described below, resulting in a primary beam current of 1.5–3.6 pA and a beam diameter of about 150-200 nm. The detailed NanoSIMS measurement parameters and tuning for specific elements can be seen in supplementary information Table S2.

The protocols developed to achieve 3D NanoSIMS analysis of the deuterium in oxides grown on zirconium alloys have been described in detail elsewhere [39], so here we provide only a brief introduction to the methodology used. During NanoSIMS experiments the primary ion beam is scanned over a selected area of the oxide surface, Figure 3, and the signals of up to 5 secondary ions with

different masses sputtered from the surface can be detected simultaneously. With typical analytical settings, a raster size of 5 × 5 μm^2 or 10 × 10 μm^2 and dwell time per pixel of 1-5 ms, a single scan of the primary beam will remove ~ 1.3 nm of the sample surface [39], and record a 2-dimensional map of the distribution of the selected ion signals from this small volume of the sample surface. This scanning process was then repeated through the depth of the oxide on each sample, resulting in a data cube with the measured values for the counts from each secondary ion signal in each pixel/voxel (Figure 3).

We have previously shown that the H_2^- signal intensity at 2 Daltons is ~7 times lower than the $^2D^-$ signal on zirconium alloys without deuteriation [39], thus the unwanted contributions to a $^2D^-$ signal from H_2^- can be ignored when analysing deuterated samples under similar experimental conditions. To collect as many $^2D^-$ counts as possible, we opened entrance slits (ES) and aperture slits (AS), which will sacrifice some mass resolution (<500) but will not affect the selection of $^2D^-$. We have previously used the $^{16}O^-$ or $^{18}O^-$ signals to locate the metal/oxide interface, but the $^{16}O^-$ ion yield from zirconium oxides can exceed 5 × 10^6 counts per second and may degrade the electron multipliers [39]. The secondary electron (SE) signals show very similar contrast of the oxide and the metal matrix to $^{16}O^-$ (see supplementary information Figure S1), and so for convenience only the SE maps are shown here to define the position of the M/O interface.

When multiple passes of the NanoSIMS primary ion beam are used to generate a 3D profile, a sputter crater is produced on the sample surface. The topography of the edges of this crater can introduce artefacts into the secondary ion signals [43], so only data from the central regions of the craters were analysed (pixels more than 0.4 μm and 0.8 μm away from the edge of the image for 5×5 μm^2 and 10×10 μm^2 raster areas respectively). ImageJ with the OpenMIMS plugin (Harvard) [44] was used to read the raw NanoSIMS data and to create deuterium depth profiles and cross-sectional views. Mercury Avizo 9.2 [45] was used for 3D data reconstruction. The methods used to present data as depth profiles, cross-section views in y-z, or x-z planes (Figure 3) and 3D reconstructions are detailed in [39].

2.3. SEM/EDX and TEM measurements

In order to allow direct correlation of the deuterium distributions measured by the NanoSIMS with the locations of small SPPs rich in alloying elements, energy dispersive X-ray (EDX) analysis was carried out at the bottom of NanoSIMS craters in a Zeiss Crossbeam 540 instrument using a 5 kV accelerating voltage to reduce beam spreading and degradation of spatial resolution. Elemental maps were generated by collecting X-ray signals for Fe (0.671 keV- 0.735 keV) and Nb (2.160 keV-2.265keV). The scan was repeated from the same region for several frames to provide high signal-to-noise ratio (SNR) maps with a total of dwell time of 2 ms/pixel for the Fe map in Figure 10 and 2.8 ms/pixel for the Nb map in Figure 11.

SEM images were also used to characterise the NanoSIMS crater surface to look for cracks. Cross-sectional TEM foils from autoclave-corroded samples containing both the oxide layer and the metal matrix were prepared using the in-situ lift-out method [46] using a Zeiss Crossbeam 540 instrument, with an initial focused ion beam milling current of 7000 pA, gradually decreasing to 300 pA at 30 kV, and further thinned to a uniform thickness of ~50 nm using a low energy beam at 2 kV and 200 pA. TEM foils from in-flux and out-of-flux samples were prepared following similar methodologies using a shielded FEI Helios Nanolab 600i FIB/SEM instrument at MRF CCFE. The oxide microstructures, and especially the nanoscale porosity, were then characterised by Fresnel contrast imaging [47] using a Jeol 2100 TEM operated at 200 kV. High-angle annular dark-field (HAADF) images were acquired using a JEOL JEM-ARM200F scanning transmission electron microscopy (STEM) operated at 200 kV.

3. Results and discussion

3.1. The microstructure of the oxide layers

The differences in the initial microstructures of the alloys described above results in different oxide microstructures generated by aqueous corrosion. Figure 4 shows typical cross-sectional TEM micrographs from all these oxides. The oxide layer thickness varies from 1.7 μm to 2.2 μm in the region of observation on the 61-day Zircaloy-4 sample Z4-1, Figure 4 (a). Even at this relatively early stage of aqueous corrosion, before the first kinetic transition, many lateral cracks 0.5-1 μm in length and 50-200 nm in width can be seen throughout the oxide. The microstructure of the oxide on Z4-2 was very similar to that on Z4-1, and is thus not shown here. The oxide layer thickness is ~1.6 μm on the Z4-pH-1 sample in the region of observation, Figure 4 (e), slightly lower than the average thickness from weight gain measurements, and 2.9 μm on the Z4-pH-2 sample, slightly higher than the average from the weight gain. The layer of large cracks on the Z4-pH-2 sample indicate that this thicker-than-average region of the oxide has gone through the kinetic transition. The oxide on the annealed Zr-1Nb sample, 1Nb-1, shows fewer and smaller cracks than Z4-1, although the oxide layer is thicker, Figure 4 (b). It is interesting to emphasize the effect of the β-Zr second phase on the interface roughness. The region with the large β–Zr running at an angle to the interface on 1Nb-1 was seen to be preferentially corroded and to result in local oxide thickness up to 4.2 μm, Figure 4 (b). Similar observations on crack distributions in oxides on commercial fuel cladding alloys have been reported in previous work [48]. High-magnification Fresnel contrast TEM images showing the distribution of oxide porosity in samples Z4-1 and 2.5Nb-4 are shown in supplementary information Figure S2. Both samples show the existence of high density of interconnected micro-cracks and nano-porosity in the outer oxide layer, while the inner oxide layer is free of porosity (or contains only a few interconnected nanopores). It is important to note that the oxide regions below these oxidised β-Zr layers in Zr-2.5Nb alloys are rather free of nanoscale porosity, see the supplementary information Figure S2 (b and d).

3.2. Deuterium distributions in oxide layers

We have divided this section into a discussion of deuterium analysis in samples of different alloy types; autoclave corroded Zircaloy-4, Zr-1Nb and Zr-2.5Nb alloys, and Zr-2.5Nb samples exposed to the in-reactor environment. Several locations were measured in each sample, and the detailed measurement parameters are given in Table S2 and all the depth profile data in supplementary Figures S3 to S7. Representative examples of these results are shown below.

Figure 5 compares the typical deuterium depth profiles and cross-sectional images selected from 3D datasets from each of the four Zircaloy-4 samples, including samples corroded in water of normal $pH_{360°C}$ = 6.15 ($pH_{25°C}$ = 7) and high $pH_{350°C}$ = 8.8. Because of the dramatic change in SE intensity when the primary ion beam reaches the underlying metal matrix, the SE signal can be used to define accurately the location of the M/O interface. The vertical solid black lines and white dashed lines show the M/O interface in the depth profiles and the cross-sectional images, respectively. All these datasets show very similar distributions of the $^{2}D^{-}$ signal in both the depth profiles and cross-sectional images; a gradually decreasing background from the oxide surface down towards the M/O interfaces and clear evidence of local deuterium trapping shown as well defined localised hot spots in the cross-sectional images and sharp peaks in the depth profiles.

Samples Z4-1 and Z4-pH-1 have the same corrosion time (61 days), a very similar corrosion temperature (360°C and 350°C) and are both at a pre-transition stage (Figure 2), and so differ only in the water pH. It is thus perhaps not surprising that the distribution of deuterium is similar in these samples. In order to define as precisely as possible how much deuterium is concentrated in the hot spots

in Figure 5, we have calculated the ratio of the summed $^2D^-$ counts in the hot spots (or sharp peaks in the depth profiles) divided by the total $^2D^-$ counts from the analysed volume, Table 1. In the samples corroded in the water of $pH_{360°C}$ = 6.15 these trapped deuterium ratios are 13% and 18% for samples Z4-1 and Z4-2 respectively, and in the high pH samples are 14% and 2% for pre-transition Z4-pH-1 and post-transition Z4-pH-2. Thus in the 3 samples before and at transition, Z4-1, Z4-2 and Z4-pH-1, the trapping ratio is similar and does not seem to depend strongly on the water pH. However, the value of trapped deuterium fraction is significantly lower in the later Z4-pH-2 sample, possibly because the corroding water has penetrated fully through cracks and porosity in the outer oxide layer, and the local deuterium hot spots are much less obvious in Figure 5 (d_1 and d_3).

In two of the datasets, Z4-2 and Z4-pH-2, there are indications of trapping of deuterium just below the M/O interface, Figure 5 (b_1 and d_1), with a significant peak also showing in the depth profile data from post-transition sample Z4-pH-2. The pre-transition samples, Z4-1 and Z4-pH-1, do not show any similar peaks below the M/O interface. This kind of peak in D signal from the underlying metal matrix has previously been attributed to the analysis of volumes of metal containing hydrides [13], and an example of the hydride distribution and morphology in the Z4-2 sample is shown in the supplementary information Figure S8. It is not surprising that we are more likely to detect hydrides near the M/O interface region in samples after longer corrosion times where the D concentration in the metallic matrix will be much higher [49, 50].

Figure 6 and 7 show a similar set of typical NanoSIMS results for the Nb-containing alloys. Figure 6 compares the depth profile and cross-sectional profiles extracted from the 3D data of deuterium distributions from autoclave-corroded alloys, while Figure 7 shows the results from Zr-2.5Nb samples 2.5Nb-3 (in-flux) and 2.5Nb-4 (out-of-flux) after in-reactor exposure at 325°C. Depth profiles at different locations are given in supplementary information Figures S5-S7 to show the reproducibility of this data. The noticeable differences to the Zircaloy-4 data shown in Figure 5 are that the number of deuterium hot spots detected in oxide layers on these materials is much lower, and in Table 1 the ratios of deuterium in the hot-spots to the total deuterium signal are also much lower than in the Zircaloy-4 samples, the highest being 2% for the out-of-flux sample 2.5Nb-4. Some evidence for weak deuterium hot spots can be seen in the data from 2.5Nb-4 in the small peaks on the plateau region of the depth profile and also close to the M/O interface. The general shape of the $^2D^-$ signals from all these samples are very similar, with broad peaks in the depth profiles. The peak of the $^2D^-$ profile is much closer to the oxide surface (W/O interface) in the in-flux sample, 2.5Nb-3, than the much broader peak observed in the out-of-flux sample, 2.5Nb-4. Another noticeable difference between Zircaloy-4 data and Zr-2.5Nb data is the existence of bright contrast features in the SE images of Zr-2.5Nb samples, Figures 6 and 7, and these features are co-located with dark contrast in the deuterium maps. EDX results (see Figure 11 in section 3.3) show these bright features in SE images are oxidised regions of original Nb-rich β-Zr, as will be discussed below.

Deuterium diffusion coefficients were calculated for all of these samples from the background profile (ignoring any localised spikes in D signal) and Fick's 2nd law as described previously [51]. The depth profiles of the three Zircaloy-4 samples before or close to the transition, Z4-1, Z4-2 and Z4-pH-1, all show a single smooth concentration profile through the whole oxide thickness under the peaks marking the hot spots, making it easy to define a region over which to calculate the diffusion coefficient values. The depth profiles from the post-transition, high pH sample, Z4-pH-2, shows two steps in the $^2D^-$ signal through the oxide thickness, Figure 5 (d_1). In the outer 0.5 μm, the signal decreases quickly, followed by a flatter region to a depth of ~1.75 μm, after which the deuterium signal decreases again down to the M/O interface. This profile is very similar to previous results reported on a post-transition Zircaloy-4 sample [52]. We interpret this kind of deuterium profile as evidence for the post-transition oxide containing an outer layer of very high porosity/cracking (the so-called fossil oxide [48]) containing many sites for trapping of the deuterium, while below 1.75 μm the oxide becomes relatively dense (the protective layer) in which hydrogen/deuterium diffusion becomes the rate-limiting

mechanism for the pickup process. As a result the diffusion coefficient was measured only in this inner part of the oxide, and a similar process was also used to define where to measure the diffusion profiles from most of the Nb alloy samples.

Averaged values of all the calculated diffusion coefficients are shown in Table 1, with the quoted error calculated from the standard deviations. Because of the complex structure of these oxide layers, with very fine grains, a high density of grain boundaries and numerous pores and different geometries of fine cracks, we do not link these calculated diffusion coefficients to a single activated transport process. More properly they are a measure of the permeability of deuterium through a highly defective nanostructure. It is also not clear which hydrogenic species preferentially diffuses/permeates through the growing oxide (D^+, OD^- or permeation by heavy water molecules [3, 7, 8, 18, 53], but the lower [D^+] in the high pH water [40] might be a factor in controlling the diffusion coefficients. However, since our samples have been corroded at different temperatures, we can also use these calculated diffusion coefficients to estimate average activation energies for permeation of deuterium, Figure 8. Although there are not very many data points for Zircaloy-4 samples, and they lie over a narrow temperature range, it seems unlikely that all of these values can be considered to lie on a single line and so be treated as if there is the same activated process for diffusion in all these samples. If we consider the rather high 1Nb-1 value as an outlier (as will be discussed below), the estimated activation energy for D diffusion (permeation) through the oxide scale for the six Nb-containing samples is 42 ± 25 kJ/mol, but for the four Zircaloy-4 samples is the remarkably higher value of 310 ± 141 kJ/mol. The range of activation energy values in zirconium oxides (monoclinic and tetragonal ZrO_2) estimated by modelling [54] is 120–200 kJ/mol. Reported experimental activation energies from different zirconium alloys lie in the range 17–150 kJ/mol as reviewed in [55]. It needs to be noticed that this wide range in experimentally measured energies can also be a result of different analytical methods used. However, if compare the values measured by the same method (e.g. the nuclear reaction analysis) on different materials, it can be seen that Zr-2.5Nb shows a much lower value (53.7 kJ/mol) than pure zirconium (100.1 kJ/mol) and Zircaloy-2 alloys (114.5 kJ/mol) [56, 57]. The data in Figure 8 also suggests that temperature dominates any variations in estimated diffusion coefficients, rather than the different water pH in which they were corroded since there is no systematic trend for the high pH samples to lie to one side of the line fitted through the data points.

Other factors that could influence the measured deuterium diffusion coefficients include the precise stage of oxidation each sample has reached, and the different starting microstructures. Previous work reports that the HPUF is not constant during oxidation, and decreases immediately before the transition in the oxidation kinetics [58, 59]. In our results we have 3 pairs of samples of the same material corroded at the same temperature, one pre- and the other at or post the kinetic transition; Z4-1 and Z4-2, Z4-pH-1 and Z4-pH-2, and 2.5Nb-1 and 2.5Nb-2. In each case the pre-transition sample shows a higher diffusion (permeation) coefficient than the sample from later in the corrosion process which correlates well with the observed decrease in HPUF.

The Zr-1Nb (1Nb-1) sample shows the highest measured D diffusion coefficient through the oxide of all the Zr-Nb samples, and even allowing for the higher corrosion temperature of 360 ºC it lies well above the fitted line for the Zircaloy-4 and Zr-2.5Nb samples, Figure 8. The pH of the corroding water is lower than used for the 2.5Nb samples, but this factor has little effect on the diffusion coefficient measured in the oxides on the Zircaloy4 samples. The most obvious difference between the Zr-1Nb and Zr-2.5Nb alloys is in the starting microstructures illustrated in Figure 1 (b and c), and specifically the different grain shape and the morphology of the β-Zr second phase. As noted above, the β-Zr forms almost continuous layers normal to the direction of oxidation in the CNL Zr-2.5Nb alloys, but large and isolated precipitates along grain boundaries in the equiaxed grain structure of the α-Zr matrix in the Zr-1Nb alloy heat treated at 720°C. These β-Zr plates then lie at random orientations to the progressing oxide growth front, Figure 4 (b). These differences in microstructure will be discussed further below.

3.3. Correlating second phases and deuterium distributions

Locations in the growing oxide layers that have been proposed for the trapping of hydrogen (deuterium) during the corrosion of zirconium alloys include SPPs [15, 17], small cracks or porosity [60, 61] and the characteristic larger cracks [62]. To address the possibility of trapping by SPPs, we stopped a NanoSIMS measurement when bright deuterium hot spots were identified in the middle of an oxide layer (about 1 µm below the surface) on sample Z4-2, and then reset the detectors to $^{52}Cr^{16}O^-$, $^{56}Fe^{16}O^-$, $^{58}Ni^{16}O^-$ and $^{120}Sn^-$ ions to determine the locations of SPPs. This experiment also required us to increase the lateral resolution and decrease the sputtering volume by selecting a smaller D1 aperture (D1-3) that also reduces the primary current from 3.6 pA to 1.5 pA. We collected data on the ion signals characteristic of the SPPs while removing about 20 nm of the sample surface and then reset the detectors back to $^2D^-$ to map the deuterium distribution again. Figure 9 (b, c, d and e) shows the location of SPPs compared to the deuterium distributions both before (a) and after (f) the SPP mapping. This data is summarised in Figure 9 (g), where solid green circles and blue dashed circles show the deuterium hot spots measured before (above) and after (below) SPP analysis respectively, and solid red circles are the locations of the SPPs. There is little correlation between the positions of the small SPPs and the deuterium hot spots.

The mapping of small SPPs with a Cs^+ primary beam means that the $^{52}Cr^{16}O^-$, $^{56}Fe^{16}O^-$ and $^{58}Ni^{16}O^-$ signal intensities are all rather low, so to be confident that we are locating the SPPs correctly we have repeated the analysis by stopping a NanoSIMS measurement when bright deuterium hot spots were identified in the middle of the oxide layer on sample Z4-1, and then analysed the exposed oxide surface by SEM/EDX mapping to determine the locations of SPPs and cracks. The SEM image in Figure 10 (a) shows an overview of the sputtering crater, and the EDX analysis in Figure 10 (b) shows the location of SPPs on the crater bottom obtained by mapping the Fe L peak (using 5 kV incident electron beam energy to achieve ~10 nm lateral and ~80 nm depth resolution [63]). Small cracks in the image are identified by white arrows, and a single larger crack marked by a white dashed circle. The secondary ion image in Figure 10 (c) is the summed $^2D^-$ counts from the sputtering in the NanoSIMS of a layer of oxide ~20 nm thick just before the EDX analysis, and the regions of enhanced deuterium counts are marked with solid white circles in Figure 10 (b and c). By comparing the locations of the SPPs in the EDX Fe map and the solid white circles of enhanced $^2D^-$ yield, it is again clear that there is no correlation in the x-y plane. Nor was any deuterium signal found associated with a large crack, the dashed circle in Figure 10 (b) which connects up towards the sample surface as shown at the left crater edge. It is possible that any deuterium trapped in these larger defects can more easily escape to the environment during storage or in the NanoSIMS vacuum. Figure 10 (d and e) are cross-sectional (x-z) images through the whole 3D NanoSIMS dataset taken along lines 1 and 2 in Figure 10 (b and c). A similar lack of correlation between the location of deuterium hotspots and SPPs was found in this vertical direction.

These results show that we cannot see any co-location of the NanoSIMS $^2D^-$ signal and the second phase particles in these Zircaloy-4 samples, and that it is more likely that deuterium is trapped preferentially at the surface of small cracks. This observation does not agree with several previous reports. Hatano et al. [17] suggested that hydrogen transport through oxide layers was via SPPs, which presumably requires preferential segregation to these features. However, the relatively poor lateral resolution of 600 µm in their experiments made it difficult to show that the much smaller intermetallic precipitates were the locations of trapped deuterium. Bossis et al. [15] interpreted SIMS measurements as showing that hydrogen was transported to the metal through large SPPs, but their 3D mapping in a CAMECA IMS-5F instrument was carried out using a 1 µm primary beam, and again it is challenging to confirm that the weak deuterium signals correspond to the position of Fe-rich precipitates that are much smaller than the beam size. The higher resolution data in Figures 9 and 10 shows that when deuterium hot spots and SPPs can be precisely positioned that there is little sign of co-location.

It is known that HPU can be profoundly affected by the choice of alloying elements in zirconium alloys, and can be especially low in Nb-containing materials [58]. In the cross-sectional images from the two autoclave-corroded Zr-2.5Nb samples in Figure 6, we detected significantly reduced $^{2}D^{-}$ counts from the regions of the SE images showing brighter contrast in Figure 6 (b_2 and c_2). A similar anti-correlation of the bright contrast and the $^{2}D^{-}$ signal can be seen in Figure 7 (b_2 and b_3). In order to be sure of the nature of these bright regions in the NanoSIMS SE images, we have carried out EDX analysis of the same area to show that these bright, D-poor regions in Figure 11 (a_1 and a_2) are rich in Nb, Figure 11 (a_3). A cross-sectional comparison of the secondary electron image and deuterium distribution in the same sample, Figure 11 (b_1 and b_2), also shows that deuterium signal is high in the region between two layers of bright linear features. From their characteristic shape, and the EDX analysis of enhanced Nb concentration, it seems consistent to identify these features as the Nb-rich residues of the β-Zr at grain boundaries in the starting microstructure of the Zr-2.5Nb samples (Figure 1). These results indicate that the Nb-rich β-Zr platess in Zr-2.5Nb alloy are probably acting as as permeation barriers for deuterium across the oxide layers.

3.4. Quantitative comparison of the trapping of deuterium in oxides

As well as the qualitative observations of the deuterium distributions, there are dramatic and systematic differences in the amount of deuterium detected in different regions of the oxides formed on these zirconium alloys. For instance, the $^{2}D^{-}$ signal intensity in hot-spots is more than three times higher than the sample average in Z4-1 and Z4-2 (Figures 5 and S3 in the supplementary information), but can rarely be detected in the Zr-2.5Nb samples, Figures 6, 7 and S5 and S6 in the supplementary information. The percentage of the total $^{2}D^{-}$ counts in each analysis that is detected in high-intensity regions (hot spots) is listed for all the samples studied in the final column in Table 1. It is evident that three of the Zircaloy-4 samples (Z4-1, Z4-2, Z4-pH-1) show much higher values than any of the Nb-containing samples, with more than 10 % of all the deuterium counts located in hot spots. The Zircaloy-4 sample after a longer corrosion time, Z4-2 (106 days), shows an even higher value than Z4-1 (61 days) which is before the transition in oxidation rate. By contrast, the post-transition high pH sample, Z4-pH-2, has a much lower hot spot trapping fraction than the pre-transition sample, Z4-pH-1. However, if we focus on the newly formed oxide near the metal/oxide interface in the Z4-pH-2 sample, the percentage of counts in the hot-spots increases to >6%. None of the Nb alloy samples shows more than 2.5% trapping, and the in-flux sample 2.5Nb-3 shows the lowest ratio (0.1 %), with almost no sign of any local trapping of deuterium in the oxide.

We also note that for the same primary beam conditions, the maximum $^{2}D^{-}$ secondary ion count from sample 2.5Nb-3 is more than ten times higher than that measured from 2.5Nb-4. The combination of higher $^{2}D^{-}$ counts (a higher concentration of deuterium in the oxide) and the higher diffusion (permeation) coefficient of deuterium through the oxide on 2.5Nb-3 correlates well with both the higher overall deuterium concentration in the metal matrix of 2.5Nb-3 (10.7 wt ppm compared with 6.4 wt ppm in 2.5Nb-4) and the deuterium pickup fractions of 4.6 % and 2.9 % respectively. This correlation, and the fact that the deuterium distributions are not uniform throughout the oxide layers, strengthens the concept that it is local permeation and trapping processes through a complex oxide microstructure that controls the overall pickup of hydrogenic species into the underlying metal matrix.

3.5. Discussion of mechanisms of deuterium permeation through the oxide layer

As has been classified by previous researchers [52], the structure of oxides grown by the aqueous corrosion of zirconium alloys can be divided into an outer, porous or fossil oxide and a relatively dense, inner protective layer. This can be seen clearly from the Fresnel contrast TEM images shown in supplementary information Figure S2. The 3D cross-sectional deuterium images in Figure 5,

6 and 7 show that in the top ~0.5 μm of the oxides on most of the samples studied here that the analysed deuterium distribution is rather uniform, presumably as a result of a high density of cracks and porosity that create preferential trap sites for deuterium. Below this the background signal is much lower, and we begin to be able to detect only local regions of intense deuterium trapping. Previous SIMS measurements show rather similar results [52, 64], but with poorer lateral and depth resolution, and were not able to resolve the smaller deuterium hot spots. If we assume that transport through the upper, porous part of the oxide is rapid, the rate-limiting step in HPU will be the penetration of hydrogen through a lower, denser layer, and the results presented above suggest that the oxides on our Zircaloy-4 samples also contain numerous local preferential trapping sites that are mostly absent in the oxides in Nb-containing alloys.

There have been several studies focused on determining the nature and distribution of small cracks and pores in oxides created by the aqueous corrosion of a wide range of zirconium alloys. TEM studies showed a variety of small crack shapes in different locations in these oxides [15, 65, 66], and the use of Fresnel imaging was introduced as a powerful technique for detecting nanoscale porosity [22]. More recently, the emphasis has shifted to the analysis of systematic differences in pore density and distribution as a function of stage of the oxidation process [38], alloy chemistry [19] and irradiation [67, 68]. This work has shown that the porosity depends on all of these parameters, and can vary significantly with the location in the oxide, but the general conclusion that can be drawn from these observations is that porosity is formed preferentially at oxide grain boundaries in most samples, and that interconnected chains of pores may be an easy path for the penetration of hydrogenic species through the growing oxide layer.

A recent study [19] reported a clear correlation between the measured increase in HPUF and the observed increase in interconnected porosity, showing that when the measured pore density at the oxide/metal interface region increased by a factor of 2, the pick-up fraction increased by a factor of 5. A detailed ab-initio molecular dynamics study [18] has also shown that the reaction of water molecules with nano-pores and nano-pipes in the oxides can play a key role in the hydrogen pickup mechanism. Figure 12 shows high-resolution 3D data on deuterium distributions from samples Z4-1 and Z4-2. Figure 12 (a and d) are magnified images of a cross-section view of the $^{2}D^{-}$ ion distribution, and the schematics in Figure 12 (b and e) shows our hypothesis for the deuterium diffusion (permeation) pathways through these oxide layers. The locations of the strong deuterium signals are marked in green, taking account of the distortion created by the SIMS analysis conditions discussed in [39], and the black bars represent potential trapping sites (small horizontal cracks) and transport paths (interconnected porosity) down towards the oxide/metal interface.

We can now discuss how the differences in oxide nano/microstructure in our set of samples can influence this permeation process. Figure 13 shows a schematic representation of the microstructure of the oxides formed on the 3 types of zirconium alloy discussed above. The substantial initial differences in the structure of the metallic matrix, especially in the distribution and nature of the Nb-rich second phase, leads to major differences in the oxide structure as well. In particular, the flat plates of the original β-Zr phase along the grain boundaries in the Zr-2.5Nb alloys are retained in the growing oxide, Figure 6 (b_2 and c_2) and Figure 7 (a_2 and b_2), and offer effective barriers to the in-diffusion of deuterium. The deuterium maps show that neither of the other two alloy microstructures (small spherical SPPs in Zircaloy-4 and larger but unaligned β-Zr plates in 1Nb-1) can offer the same almost continuous permeation barrier between the corroding medium and the metal matrix, Figures 10 and 11.

These Nb-rich regions in the 1% and 2.5% Nb alloys are no longer the high temperature β-Zr phase after prolonged treatments at temperatures well below the monotectoid, but are decomposing to the equilibrium phases, α-Zr, ω-Zr and β-Nb [69]. The complex mixture of phases formed by this decomposition reaction is illustrated by the STEM image in Figure 13 (d). It is this complex microstructure in the Zr- 2.5Nb alloys through which the deuterium generated by the corrosion process

must penetrate to reach the underlying metal matrix. From the deuterium maps in Figures 6 and 7 it is clear that these regions are not acting as traps since the deuterium concentrations in these features are always lower than in the surrounding oxide, but as permeation barriers. We can speculate that the local electric fields generated by the excess of Nb^{5+} ions as these regions are oxidised [29], or more slowly oxidising β-Nb nanoparticles on the oxide grain boundaries may play a part in providing this barrier effect.

Another factor we must consider is the dominant transport mechanisms for deuterium through these oxide layers. The very low measured activation energy for the diffusion (permeation) of deuterium through the oxides on the Zr-2.5Nb alloys is difficult to correlate with the observed low HPUF values in Table 1. This apparent conflict can be reconciled if we combine the observed blocking effect of the residual β-Zr layers and their detailed microstructure shown in Figure 12. The dense local porosity created during the decomposition/oxidation process offers low activation transport pathways but the limited area of these pores in an otherwise impermeable layer reduces the overall flux of hydrogenic species, in a manner analogous to the well-known phenomenon of grain boundary diffusion in polycrystalline microstructures [70]. The oxide regions between these Nb-rich layers are rather free of nanoscale porosity (supplementary Figure S2), and contain rather high concentrations of deuterium (Figure 7), but are not the rate-limiting regions for the permeation process. The oxides on Zircaloy-4 samples contain porosity throughout the inner protective layer that offers the primary pathways for deuterium in-diffusion, but although these pores are present on essentially every grain boundary (leading to a high flux) they are not as well connected as in the Nb-rich regions of the Zr-2.5Nb alloys, and so the overall activation barrier measured is higher.

4. Conclusions

3D deuterium distributions have been measured in the oxides formed on different zirconium alloys, Zircaloy-4 in pure water and a high pH environment, and Zr-1Nb and Zr-2.5Nb alloys under autoclave and in-reactor conditions. The main conclusions are:

1. For pre-transition Zircaloy-4 samples, the deuterium is highly concentrated in the fossil oxide near the water/oxide interface, and there is a gradual decrease in trapped deuterium in the denser oxide towards the M/O interface with abrupt peaks in the $^{2}D^{-}$ signal that is evidence for strong local trapping sites.
2. The high temperature annealed Zr-1Nb sample shows a similar deuterium diffusion profile as the pre-transition Zircaloy samples, but the Zr-2.5Nb samples with a different initial microstructure, show deuterium distributions with little sign of strong local trapping.
3. Combining NanoSIMS and SEM/EDX analysis on the same surface, we can demonstrate that deuterium is not preferentially trapped at SPPs consumed by the oxide, but there is direct evidence for trapping at the surfaces of small cracks.
4. The fraction of the total deuterium in the oxide trapped in local hot spots has been calculated for the different materials. Zircaloy-4 samples show a much higher trapped fraction than either Zr-1Nb or Zr-2.5Nb samples. This local trapping offers a way to increase the concentration of deuterium in the oxide, and offers an explanation for the higher deuterium (hydrogen) pick-up fractions measured in Zircaloy-4 samples.
5. The diffusion (permeation) coefficients of deuterium in all the oxides were calculated, and show activation energy values that are much higher in oxides on Zircaloy-4 than the Zr-2.5Nb alloys. We have suggested an explanation for this based on the different oxide microstructures formed on these alloys.
6. Both the deuterium concentration and the deuterium diffusion coefficients in the oxide on the in-flux Zr-2.5Nb sample is higher than for the out-of-flux sample in water of the same chemistry. This is direct evidence that irradiation can increase the rate of key

mechanisms controlling transport of deuterium through the oxide, and influence both the concentration of deuterium in the metal matrix and the deuterium pick-up fractions.

7. 3D mapping of deuterium hot-spots at high resolution provides unique mechanistic information on the mechanisms of hydrogen uptake during the corrosion of zirconium. We suggest the shape of the deuterium paths mapped in the oxide show that the development of interconnected porosity along oxide grain boundaries (as shown in previous TEM analysis) is the critical rate-determining mechanism that controls HPU in the aqueous corrosion of zirconium alloys.
8. We have shown by deuterium mapping that the characteristic microstructure of the Zr-2.5Nb alloys with β-Zr plates at the grain boundaries lying perpendicular to the direction of oxide growth and deuterium penetration leads to a blocking effect on the deuterium flux, and may be an important factor determining the improved resistance to HPU in these alloys.

Acknowledgements

The authors acknowledge the contribution made to this work by their collaborators from Westinghouse, Canadian Nuclear Laboratories and the MUZIC project providing zirconium samples. This study is funded by the UK Engineering and Physical Sciences Research Council under grant EP/M018237/1. Some of the work was done using UKAEA's Materials Research Facility, which has been funded by the UK's National Nuclear User Facility and Henry Royce Institute initiative. EPSRC grants (EP/K040375/1 and EP/N010868/1) are acknowledged for funding the 'South of England Analytical Electron Microscope' and the Zeiss Crossbeam FIB/SEM used in this research. Junliang Liu is grateful for support from the EPSRC grant (EP/P001645/1). Thomas Aarholt is grateful for support from Westinghouse. Alistair Garner and Michael Preuss are grateful for funding from the UK Engineering and Physical Sciences Research Council under grant EP/L018616/1 and EP/I005420/1. The authors acknowledge Prof. James Marrow for the provision of facilities to create 3D images using the Avizo software.

References

[1] B. Cox, A mechanism for the hydrogen uptake process in zirconium alloys, J Nucl Mater 264(3) (1999) 283-294.
[2] D. Northwood, U. Kosasih, Hydrides and delayed hydrogen cracking in zirconium and its alloys, International Metals Reviews 28(1) (1983) 92-121.
[3] B. Malki, O. Le Bacq, A. Pasturel, Ab initio study of hydrogen related defect in ZrO2: consequences on dry and aqueous oxidation, J Journal of Nuclear Materials 416(3) (2011) 362-368.
[4] B. Malki, O. Le Bacq, A. Pasturel, Role of water on the stability of oxygen vacancies in ZrO2: An ab initio based study, J Nucl Mater 429(1-3) (2012) 173-176.
[5] M.S. Veshchunov, A.V. Berdyshev, Modelling of hydrogen absorption by zirconium alloys during high temperature oxidation in steam, J Nucl Mater 255(2-3) (1998) 250-262.
[6] B. Cox, Y.M. Wong, A hydrogen uptake micro-mechanism for Zr alloys, J Nucl Mater 270(1-2) (1999) 134-146.
[7] R. Sato, S. Ohkuma, Y. Shibuta, F. Shimojo, S. Yamaguchi, Proton migration on hydrated surface of cubic ZrO2: Ab initio molecular dynamics simulation, The Journal of Physical Chemistry C 119(52) (2015) 28925-28933.
[8] R. Vieira, R. Vilão, A. Marinopoulos, P. Gordo, J. Paixão, H. Alberto, J. Gil, A. Weidinger, R. Lichti, B. Baker, Isolated hydrogen configurations in zirconia as seen by muon spin spectroscopy and ab initio calculations, Phys Rev B 94(11) (2016) 115207.
[9] M. Lindgren, G. Sundell, I. Panas, L. Hallstadius, M. Thuvander, Andr, eacute, H.-O. n, Toward a Comprehensive Mechanistic Understanding of Hydrogen Uptake in Zirconium Alloys by Combining Atom Probe Analysis With Electronic Structure Calculations, in: B. Comstock, P. Barberis (Eds.), ASTM International, West Conshohocken, PA, 2015, pp. 515-539.
[10] K. Li, J. Liu, C.R. Grovenor, K.L. Moore, NanoSIMS imaging and analysis in materials science, Annual Review of Analytical Chemistry 13 (2020) 273-292.
[11] A.J. Maroto, R. Bordoni, M. Villegas, A.M. Olmedo, M. Blesa, A. Iglesias, P. Koenig, Growth and characterization of oxide layers on zirconium alloys, J Nucl Mater 229(1) (1996) 79-92.
[12] S.S. Yardley, K.L. Moore, N. Ni, J.F. Wei, S. Lyon, M. Preuss, S. Lozano-Perez, C.R.M. Grovenor, An investigation of the oxidation behaviour of zirconium alloys using isotopic tracers and high resolution SIMS, J Nucl Mater 443(1-3) (2013) 436-443.
[13] M.B. Elmoselhi, B.D. Warr, S. McIntyre, A Study of the Hydrogen Uptake Mechanism in Zirconium Alloys, in: A.M. Garde, E.R. Bradley (Eds.), ASTM International, West Conshohocken, PA, 1994, pp. 62-79.
[14] K. Une, K. Sakamoto, J. Matsunaga, Y. Etoh, M. Aomi, I. Takagi, K. Sawada, H. Watanabe, Controlling factors in hydrogen absorption of zirconium alloys, Proceedings of TopFuel (2012) 2-6.
[15] P. Bossis, Leli, egrave, G. vre, P. Barberis, X. Iltis, F. Lefebvre, Multi-Scale Characterization of the Metal-Oxide Interface of Zirconium Alloys, in: G.P. Sabol, G.D. Moan (Eds.), ASTM International, West Conshohocken, PA, 2000, pp. 918-945.
[16] K. Baur, F. Garzarolli, H. Ruhmann, H.J. Sell, Electrochemical Examinations in 350C Water with Respect to the Mechanism of Corrosion-Hydrogen Pickup, in: G.P. Sabol, G.D. Moan (Eds.), ASTM International, West Conshohocken, PA, 2000, pp. 836-852.
[17] Y. Hatano, K. Isobe, R. Hitaka, M. Sugisaki, Role of intermetallic precipitates in hydrogen uptake of Zircaloy-2, J Nucl Sci Technol 33(12) (1996) 944-949.
[18] J. Hu, J. Liu, S. Lozano-Perez, C.R.M. Grovenor, M. Christensen, W. Wolf, E. Wimmer, E.V. Mader, Hydrogen pickup during oxidation in aqueous environments: The role of nano-pores and nano-pipes in zirconium oxide films, Acta Mater 180 (2019) 105-115.
[19] A. Couet, L. Borrel, J. Liu, J. Hu, C. Grovenor, An integrated modeling and experimental approach to study hydrogen pickup mechanism in zirconium alloys, Corros Sci 159 (2019) 108134.
[20] G. Sundell, M. Thuvander, A. Yatim, H. Nordin, H.-O. Andrén, Direct observation of hydrogen and deuterium in oxide grain boundaries in corroded Zirconium alloys, Corros Sci 90 (2015) 1-4.
[21] A. Garner, J. Hu, A. Harte, P. Frankel, C. Grovenor, S. Lozano-Perez, M. Preuss, The effect of Sn concentration on oxide texture and microstructure formation in zirconium alloys, Acta Mater 99 (2015) 259-272.

[22] N. Ni, S. Lozano-Perez, M.L. Jenkins, C. English, G.D.W. Smith, J.M. Sykes, C.R.M. Grovenor, Porosity in oxides on zirconium fuel cladding alloys, and its importance in controlling oxidation rates, Scripta Mater 62(8) (2010) 564-567.
[23] J. Hu, B. Setiadinata, T. Aarholt, A. Garner, A. Vilalta-Clemente, J.M. Partezana, P. Frankel, P. Bagot, S. Lozano-Perez, A. Wilkinson, M. Preuss, M. Moody, C. Grovenor, Understanding Corrosion and Hydrogen Pickup of Zirconium Fuel Cladding Alloys: The Role of Oxide Microstructure, Porosity, Suboxides, and Second-Phase Particles, in: R. Comstock, A. Motta (Eds.), ASTM International, West Conshohocken, PA, 2018, pp. 93-126.
[24] J. Liu, H. Yu, P. Karamched, J. Hu, G. He, D. Goran, G.M. Hughes, A.J. Wilkinson, S. Lozano-Perez, C.R.M. Grovenor, Mechanism of the α-Zr to hexagonal-ZrO transformation and its impact on the corrosion performance of nuclear Zr alloys, Acta Mater 179 (2019) 328-341.
[25] N. Ni, D. Hudson, J. Wei, P. Wang, S. Lozano-Perez, G.D.W. Smith, J.M. Sykes, S.S. Yardley, K.L. Moore, S. Lyon, R. Cottis, M. Preuss, C.R.M. Grovenor, How the crystallography and nanoscale chemistry of the metal/oxide interface develops during the aqueous oxidation of zirconium cladding alloys, Acta Mater 60(20) (2012) 7132-7149.
[26] B. de Gabory, Y. Dong, A.T. Motta, E.A. Marquis, EELS and atom probe tomography study of the evolution of the metal/oxide interface during zirconium alloy oxidation, J Nucl Mater 462 (2015) 304-309.
[27] J. Hu, A. Garner, N. Ni, A. Gholinia, R.J. Nicholls, S. Lozano-Perez, P. Frankel, M. Preuss, C.R.M. Grovenor, Identifying suboxide grains at the metal-oxide interface of a corroded Zr-1.0%Nb alloy using (S)TEM, transmission-EBSD and EELS, Micron 69 (2015) 35-42.
[28] J. Liu, G. He, J. Hu, Z. Shen, M. Kirk, M. Li, E. Ryan, P. Baldo, S. Lozano-Perez, C. Grovenor, Irradiation-induced amorphization in the zirconium suboxide on Zr-0.5Nb alloys, J Nucl Mater 513 (2019) 226-231.
[29] A. Couet, A.T. Motta, A. Ambard, The coupled current charge compensation model for zirconium alloy fuel cladding oxidation: I. Parabolic oxidation of zirconium alloys, Corros Sci 100 (2015) 73-84.
[30] A. Couet, A.T. Motta, A. Ambard, D. Livigni, In-situ electrochemical impedance spectroscopy measurements of zirconium alloy oxide conductivity: Relationship to hydrogen pickup, Corros Sci 119 (2017) 1-13.
[31] M.P. Moody, A. Vella, S.S.A. Gerstl, P.A.J. Bagot, Advances in atom probe tomography instrumentation: Implications for materials research, Mrs Bull 41(1) (2016) 40-45.
[32] G. Sundell, M. Thuvander, H.O. Andren, Barrier oxide chemistry and hydrogen pick-up mechanisms in zirconium alloys, Corros Sci 102 (2016) 490-502.
[33] R. Gemma, T. Al-Kassab, R. Kirchheim, A. Pundt, Analysis of deuterium in V-Fe5at.% film by atom probe tomography (APT), J Alloy Compd 509 (2011) S872-S876.
[34] D. Haley, S.V. Merzlikin, P. Choi, D. Raabe, Atom probe tomography observation of hydrogen in high-Mn steel and silver charged via an electrolytic route, Int J Hydrogen Energ 39(23) (2014) 12221-12229.
[35] K.L. Moore, M. Schröder, C.R. Grovenor, Imaging secondary ion mass spectroscopy, Handbook of Nanoscopy, Volume 1&2 2 (2012) 709-744.
[36] W. Jiang, S.R. Spurgeon, Z. Zhu, X. Yu, K. Kruska, T. Wang, J. Gigax, L. Shao, D.J. Senor, Chemical imaging and diffusion of hydrogen and lithium in lithium aluminate, J Nucl Mater 511 (2018) 1-10.
[37] J.-H. Shim, J. Lee, S.Y. Han, S. Lee, Synergistic effects of coating and doping for lithium ion battery cathode materials: synthesis and characterization of lithium titanate-coated LiCoO2 with Mg doping, Electrochim Acta 186 (2015) 201-208.
[38] J. Hu, T. Aarholt, B. Setiadinata, K. Li, A. Garner, S. Lozano-Perez, M. Moody, P. Frankel, M. Preuss, C. Grovenor, A multi-technique study of "barrier layer" nano-porosity in Zr oxides during corrosion and hydrogen pickup using (S) TEM, TKD, APT and NanoSIMS, Corros Sci (2019) 108109.
[39] K. Li, T. Aarholt, J. Liu, H. Hulme, A. Garner, M. Preuss, S. Lozano-Perez, C. Grovenor, 3D-characterization of deuterium distributions in zirconium oxide scale using high-resolution SIMS, Appl Surf Sci 464 (2019) 311-320.
[40] J. Sayers, S. Lozano-Perez, R.J. Nicholls, S. Ortner, A high-resolution characterization of the oxide-metal interface in Zircaloy-4 and its relation to the oxidation and hydrogen pickup mechanisms, J Nucl Mater 525 (2019) 72-82.

[41] A.J.G. Maroto, R. Bordoni, M. Villegas, A.M. Olmedo, M.A. Blesa, A. Iglesias, P. Koenig, Growth and characterization of oxide layers on zirconium alloys, J Nucl Mater 229 (1996) 79-92.
[42] J. Liu, High resolution structural analysis of irradiated zirconium alloys, Department of Materials, University of Oxford, 2019.
[43] C.W. Magee, R.E. Honig, Depth profiling by SIMS—depth resolution, dynamic range and sensitivity, Surf Interface Anal 4(2) (1982) 35-41.
[44] C. Poczatek, Z. Kaufman, C. Lechene, OpenMIMS ImageJ Plugin Guide, Harvard Medical School (Boston, Massachusetts, USA) (2009) 1-18.
[45] ThermoFisher, https://www.fei.com/software/amira-avizo/. 2018).
[46] S. Lozano-Perez, A guide on FIB preparation of samples containing stress corrosion crack tips for TEM and atom-probe analysis, Micron 39(3) (2008) 320-328.
[47] M. Rühle, M. Wilkens, Defocusing contrast of cavities, Crystal Lattice Defects 6(3) (1975) 129-140.
[48] N. Ni, S. Lozano-Perez, J.M. Sykes, G.D.W. Smith, C.R.M. Grovenor, Focussed ion beam sectioning for the 3D characterisation of cracking in oxide scales formed on commercial ZIRLO (TM) alloys during corrosion in high temperature pressurised water, Corros Sci 53(12) (2011) 4073-4083.
[49] K. Une, S. Ishimoto, Dissolution and precipitation behavior of hydrides in Zircaloy-2 and high Fe Zircaloy, J Nucl Mater 322(1) (2003) 66-72.
[50] J.J. Kearns, Terminal solubility and partitioning of hydrogen in the alpha phase of zirconium, Zircaloy-2 and Zircaloy-4, J Nucl Mater 22(3) (1967) 292-303.
[51] M. Tupin, C. Bisor, P. Bossis, J. Chene, J.L. Bechade, F. Jomard, Mechanism of corrosion of zirconium hydride and impact of precipitated hydrides on the Zircaloy-4 corrosion behaviour, Corros Sci 98 (2015) 478-493.
[52] M. Tupin, F. Martin, C. Bisor, R. Verlet, P. Bossis, J. Chene, F. Jomard, P. Berger, S. Pascal, N. Nuns, Hydrogen diffusion process in the oxides formed on zirconium alloys during corrosion in pressurized water reactor conditions, Corros Sci 116 (2017) 1-13.
[53] T. Smith, Kinetics and mechanism of hydrogen permeation of oxide films on zirconium, J Nucl Mater 18(3) (1966) 323-336.
[54] H. Muta, Y. Etoh, Y. Ohishi, K. Kurosaki, S. Yamanaka, Ab initio study of hydrogen diffusion in zirconium oxide, J Nucl Sci Technol 49(5) (2012) 544-550.
[55] I. Takagi, K. Une, S. Miyamura, T. Kobayashi, Deuterium diffusion in steam-corroded oxide layer of zirconium alloys, J Nucl Mater 419(1-3) (2011) 339-346.
[56] D. Khatamian, F.D. Manchester, An ion beam study of hydrogen diffusion in oxides of Zr and Zr-Nb (2.5 wt%): I. Diffusion parameters for dense oxide, J Nucl Mater 166(3) (1989) 300-306.
[57] D. Khatamian, Hydrogen diffusion in oxides formed on surfaces of zirconium alloys, J Alloy Compd 253-254 (1997) 471-474.
[58] A. Coueta, A.T. Motta, R.J. Comstock, Hydrogen pickup measurements in zirconium alloys: Relation to oxidation kinetics, J Nucl Mater 451(1-3) (2014) 1-13.
[59] A.T. Motta, A. Couet, R.J. Comstock, Corrosion of Zirconium Alloys Used for Nuclear Fuel Cladding, Annu Rev Mater Res 45 (2015) 311-343.
[60] N. Ramasubramanian, V. Perovic, M. Leger, Hydrogen Transport in the Oxide and Hydrogen Pickup by the Metal During Out- and In-Reactor Corrosion of Zr-2.5Nb Pressure Tube Material, in: G.P. Sabol, G.D. Moan (Eds.), ASTM International, West Conshohocken, PA, 2000, pp. 853-876.
[61] Y. Nishino, M. Endo, E. Ibe, T. Yasuda, Formation and dissolution of oxide film on zirconium alloys in 288 degrees C pure water under gamma-ray irradiation, J Nucl Mater 248 (1997) 292-298.
[62] B. Cox, Y.-M. Wong, A hydrogen uptake micro-mechanism for Zr alloys, J Nucl Mater 270(1) (1999) 134-146.
[63] D. Drouin, A.R. Couture, D. Joly, X. Tastet, V. Aimez, R. Gauvin, CASINO V2. 42—A Fast and Easy-to-use Modeling Tool for Scanning Electron Microscopy and Microanalysis Users, Scanning 29(3) (2007) 92-101.
[64] A.T. Motta, A. Yilmazbayhan, R.J. Comstock, J. Partezana, G.P. Sabol, B. Lai, Z. Cai, Microstructure and Growth Mechanism of Oxide Layers Formed on Zr Alloys Studied with Micro-Beam Synchrotron Radiation, in: P. Rudling, B. Kammenzind (Eds.), ASTM International, West Conshohocken, PA, 2005, pp. 205-232.

[65] A. Yilmazbayhan, E. Breval, A.T. Motta, R.J. Comstock, Transmission electron microscopy examination of oxide layers formed on Zr alloys, J Nucl Mater 349(3) (2006) 265-281.
[66] K. Takeda, H. Anada, Mechanism of Corrosion Rate Degradation Due to Tin, in: G.P. Sabol, G.D. Moan (Eds.), ASTM International, West Conshohocken, PA, 2000, pp. 592-608.
[67] J. Hu, A. Garner, P. Frankel, M. Li, M.A. Kirk, S. Lozano-Perez, M. Preuss, C. Grovenor, Effect of neutron and ion irradiation on the metal matrix and oxide corrosion layer on Zr-1.0Nb cladding alloys, Acta Mater 173 (2019) 313-326.
[68] J. Liu, G. He, Anne Callow, K. Li, S. Lozano-Perez, A.J. Wilkinson, M. Moody, C.R.M. Grovenor, J. Hu, M. Kirk, M. Li, A.H. Mir, J. Hinks, S. Donnelly, J. Partezana, H. Nordin, Ex-situ and in-situ studies of radiation damage mechanisms in Zr-Nb alloys, 19th International Symposium, ASTM International, 2019, p. Accepted.
[69] C.D. Cann, E.E. Sexton, A.M. Duclos, G.G. Smith, The effect of decomposition of beta-phase Zr-20 at% Nb on hydrogen partitioning with alpha-zirconium, J Nucl Mater 210(1) (1994) 6-10.
[70] Y. Mishin, C. Herzig, Grain boundary diffusion: recent progress and future research, Materials Science and Engineering: A 260(1) (1999) 55-71.

Tables

Table 1. Sample alloys and oxidation conditions. T is the corrosion temperature; $C_{H\ or\ D}$ is the hydrogen/deuterium concentration in each alloy; D_c is the hydrogen/deuterium diffusion coefficient in the oxide, the error is the standard deviation.

ID	Alloy	T	Oxidation (days)			pH[a)]	Oxide thickness	Corrosion conditions	C_D[b)]	D_c	H/D pickup fraction	$^2D^-$ ion Hot-spots/Total
		(°C)	100% H_2O	100% D_2O	50% D_2O		μm		wt ppm	m^2/s	%	%
Z4-1	Zircaloy-4	360	30	31	-	7	1.9	Autoclave		$2.5\pm1.0\times10^{-20}$	3.3	13.0±0.2
Z4-2	Zircaloy-4	360	75	31	-	7	2.2	Autoclave		$1.4\pm0.6\times10^{-20}$	10.9	18.0±0.3
Z4-pH-1	Zircaloy-4	350	-	-	61	8.8	1.5	Autoclave		$1.0\pm0.6\times10^{-20}$	-	14.0
Z4-pH-2	Zircaloy-4	350	-	-	147	8.8	2.9	Autoclave		$5.3\pm2.9\times10^{-21}$	-	2.0±0.7 (6.6±3.0)[c)]
1Nb-1 [d)]	Annealed Zr-1Nb	360	15	31	-	7	2.4	Autoclave		$4.6\pm2.1\times10^{-20}$	4.2	1.4±1.3
2.5Nb-1	Zr-2.5Nb	300	-	150	-	10.5	1.9	Autoclave	1.2	$2.4\pm3.2\times10^{-21}$	1.6	0.7±0.1
2.5Nb-2	Zr-2.5Nb	300	-	700	-	10.5	3.7	Autoclave	4.4	$5.9\pm4.1\times10^{-22}$	3.1	1.5
2.5Nb-3	Zr-2.5Nb	325	-	192	-	10.5	2.5	In-flux	10.7	$5.2\pm3.0\times10^{-21}$	4.6	0.1
2.5Nb-4	Zr-2.5Nb	325	-	185	--	10.5	2.4	Out-of-flux	6.4	$1.2\pm0.2\times10^{-21}$	2.9	2.0

[a)] pH values of Z4-1, Z4-2 and 1Nb-1 samples were measured at 360°C, Z4-pH-1 and Z4-pH-2 at 350°C, and 2.5Nb-1-4 at 25°C.
[b)] Deuterium contents of 2.5Nb 1-4 samples were measured by the Hydrogen Hot-Gas Extraction (HHEG) at CNL.
[c)] Only consider the deuterium in the newly formed oxide layer (within 1μm from the metal/oxide interface) in the Z4-pH-2 sample.
[d)] Zr-1%Nb (1Nb-1) annealed at 720 ºC for 24 hours to form the Nb-rich β-Zr phase.

Figures

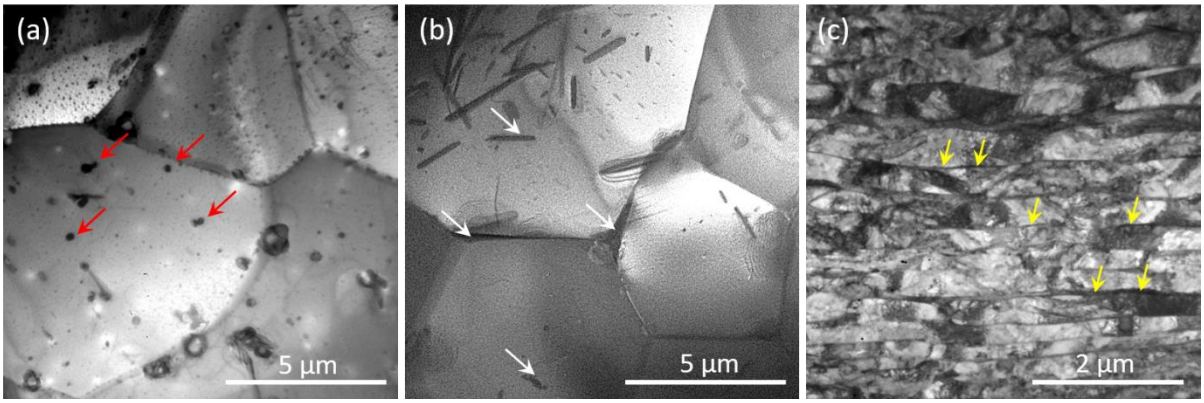

Figure 1. TEM images showing starting microstructures of the different alloys studied, (a) Zircaloy-4 containing small SPPs, (b) annealed Zr-1Nb containing large β-Zr precipitates, and (c) CNL Zr-2.5Nb. The arrows highlight the different morphologies of second phases in these three materials.

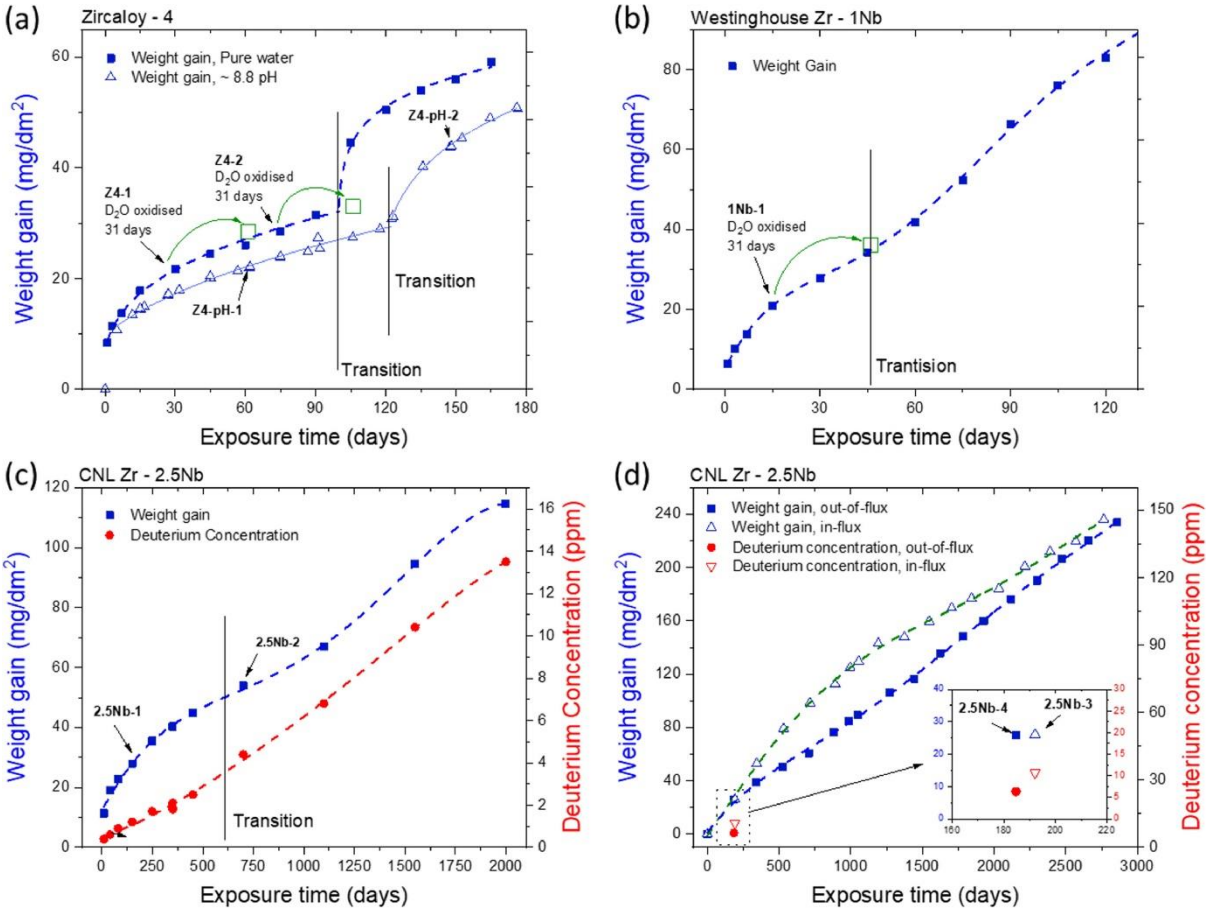

Figure 2. Weight gain and deuterium concentration (CNL_Zr-2.5Nb samples) as a function of corrosion time for the sample sets from which the specimens were chosen for this study. The vertical black lines show the approximate position of the acceleration of oxidation rate at the transition point. In (a) and (b), the green squares indicate samples after a second corrosion stage of 31 days in D_2O shown by the green arrows.

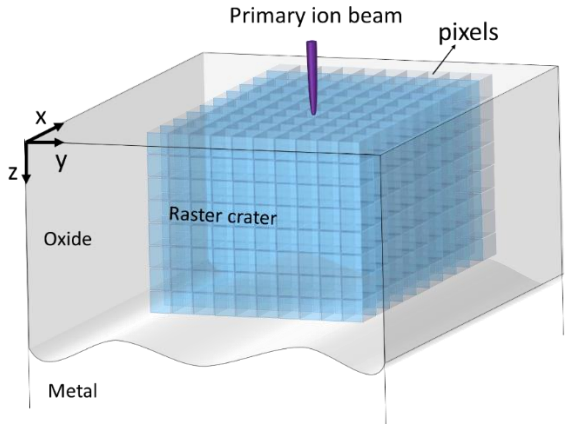

Figure 3. The geometry of NanoSIMS measurements for depth-profile through an oxide layer.

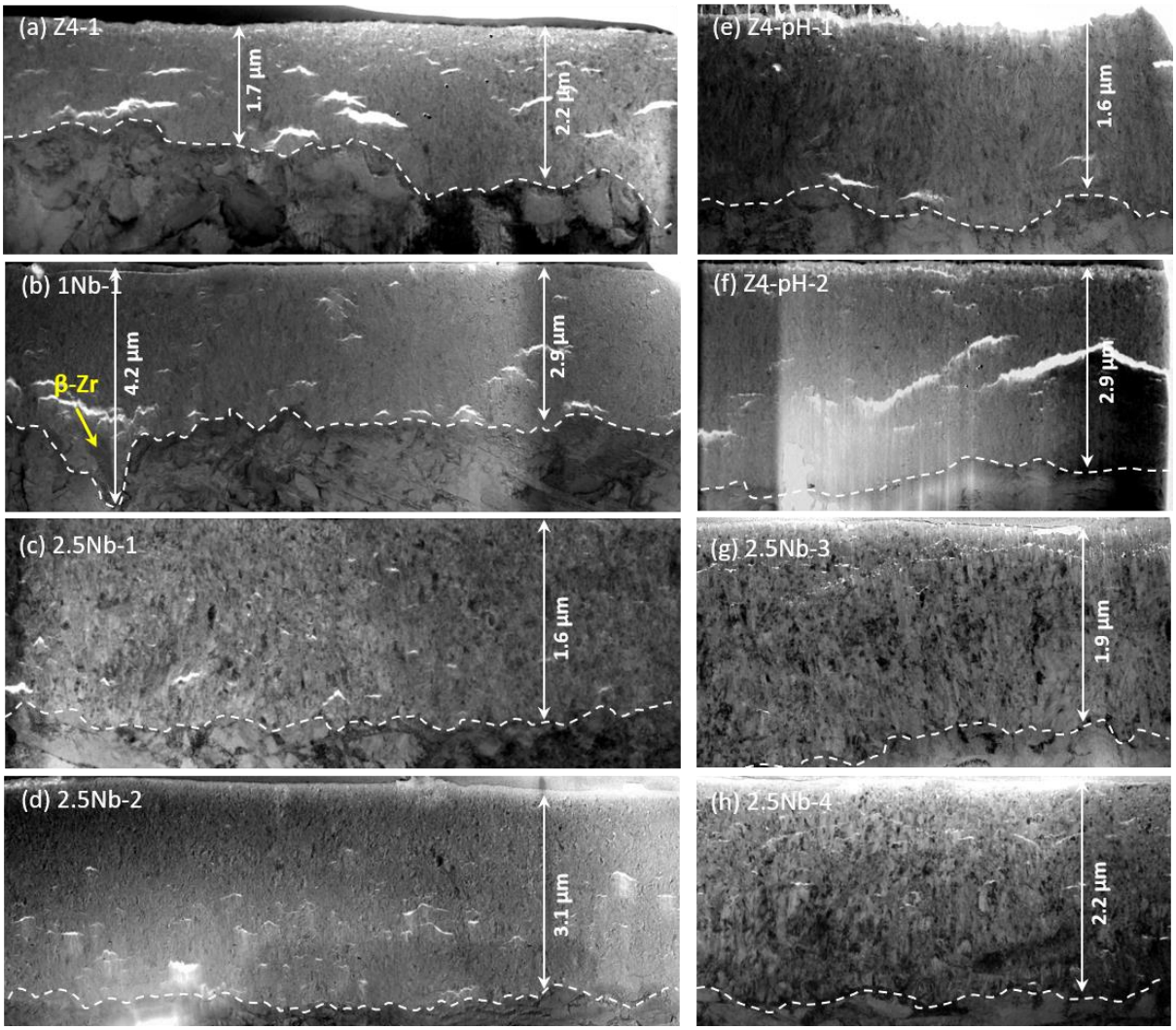

Figure 4. TEM cross-sectional images of the oxide microstructure in the samples studied by NanoSIMS analysis. (a) Z4-1, (b) 1Nb-1, (c) 2.5Nb-1, (d) 2.5Nb-2, (e) Z4-pH-1, (f) Z4-pH-2, (g) 2.5Nb-3 and (h) 2.5Nb-4 samples. White dashed lines mark the position of the metal/oxide interface. The Z4-2 oxide looked very similar to that on Z4-1 in (a), and so is not shown here.

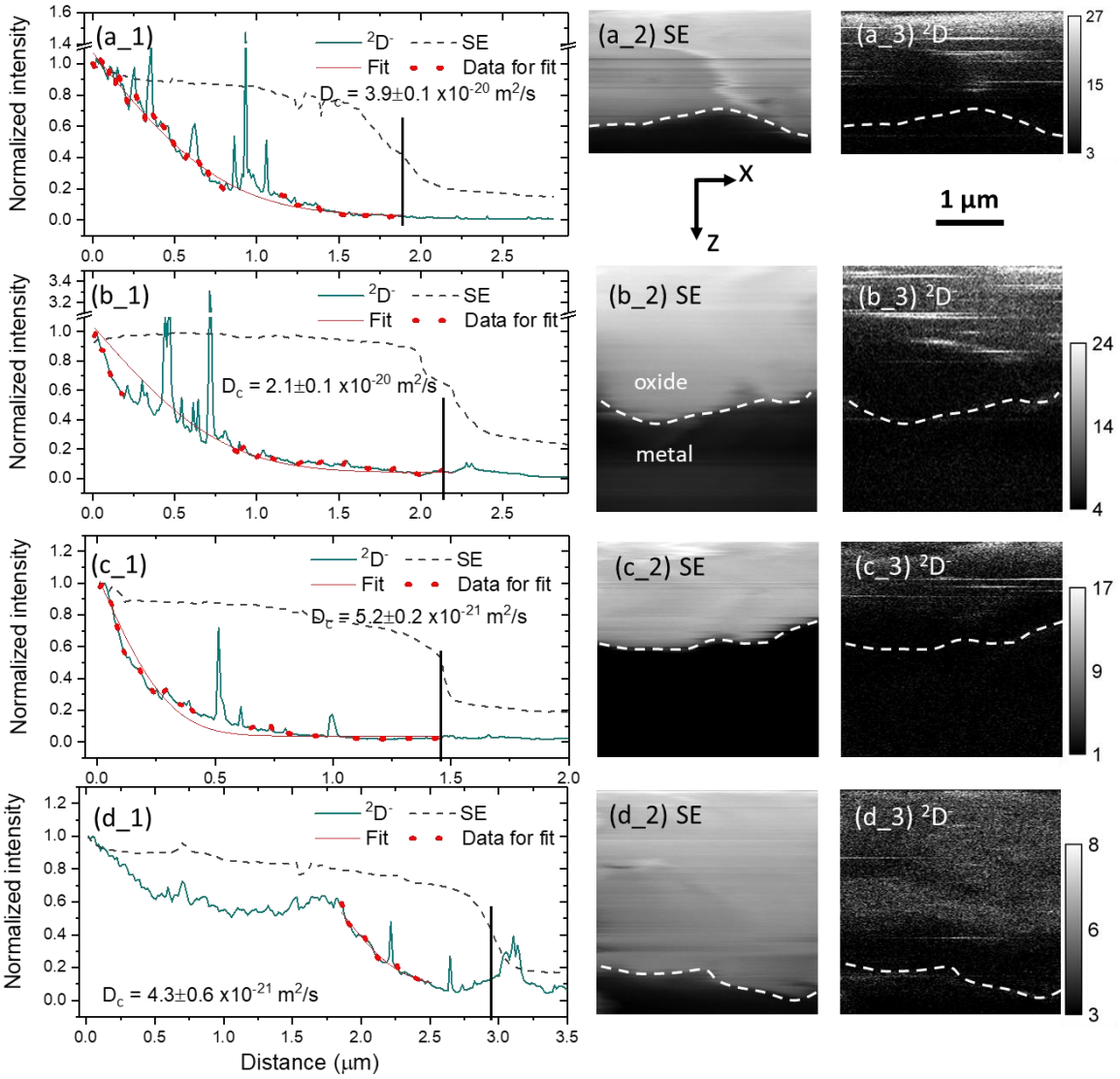

Figure 5. Depth profile and a cross-sectional view of 3D data from samples Z4-1, Z4-2, Z4-pH-1 and Z4-pH-2 in panels a_x, b_x, c_x and d_x, respectively. 1, 2 and 3 represent the depth profile plot, cross-section view of secondary ion image and the cross-sectional view of the secondary ion $^2D^-$ signal respectively, all extracted from the 3D data. The intensities of $^2D^-$ and secondary electron signals were normalised by the intensity at the surface (at 0 μm), and the vertical black lines on the depth profile and white dashed lines on the cross-sectional images mark the position of the metal/oxide interface. Fitting the diffusion coefficients of deuterium through the oxide was carried out using Fick's 2nd law on the sections of the depth profiles marked with dots. The depth profile data in images (a_1) and (b_1) are reprinted from Figure 5 in [39], Copyright (2019), with permission from Elsevier.

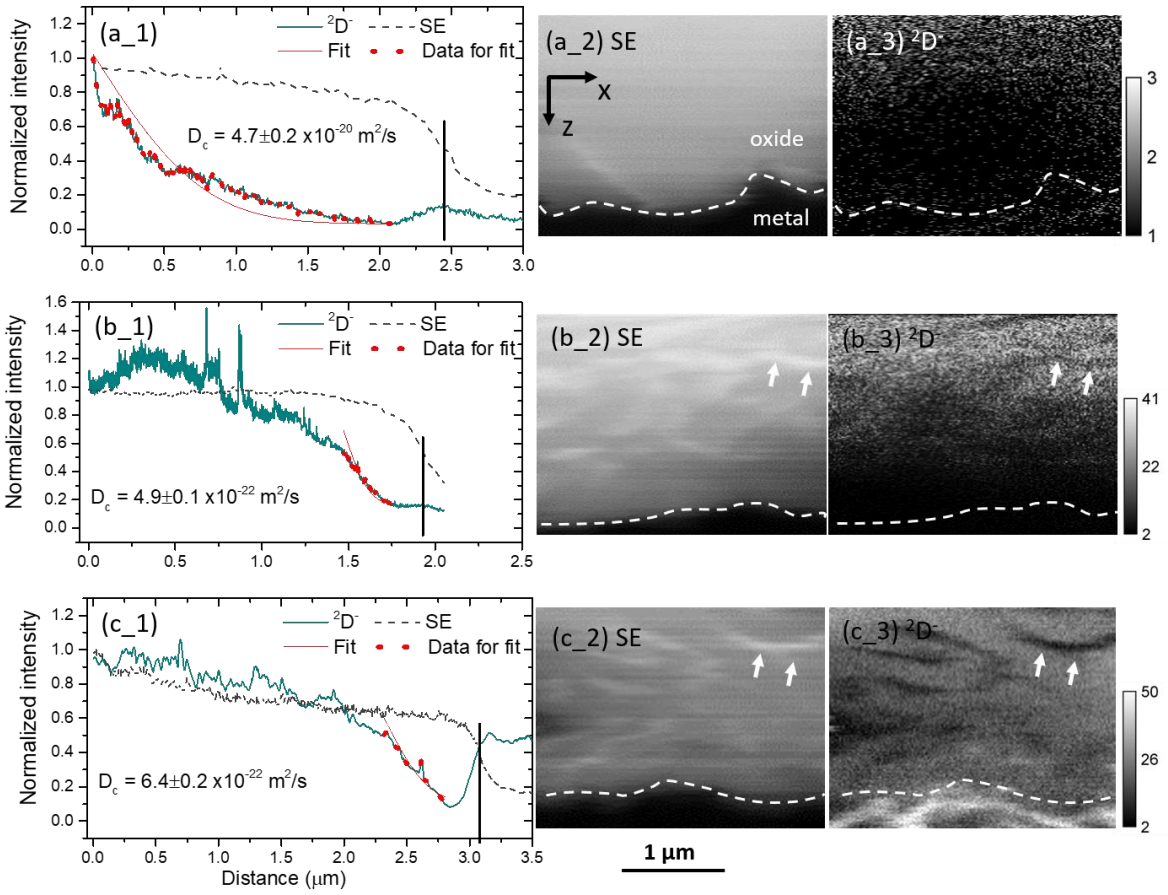

Figure 6. Depth profile and cross-sectional views of 3D data from samples 1Nb-1, 2.5Nb-1 and 2.5Nb-2 samples in panels a_x, b_x and c_x, respectively. 1, 2 and 3 represent the depth profile plot, cross-section view of secondary ion image and the cross-sectional view of the secondary ion $^2D^-$ signal respectively, all extracted from the 3D data. The intensities of $^2D^-$ and secondary electron signals were normalised by the intensity at the surface (at 0 μm), and the vertical black lines on the depth profile and white dashed lines on the cross-sectional images mark the position of the metal/oxide interface. Fitting the diffusion coefficients of deuterium through the oxide was carried out using Fick's 2nd law on the sections of the depth profiles marked with dots. The white arrows in the SE and $^2D^-$ maps mark the original locations of the Nb-rich β-Zr phase.

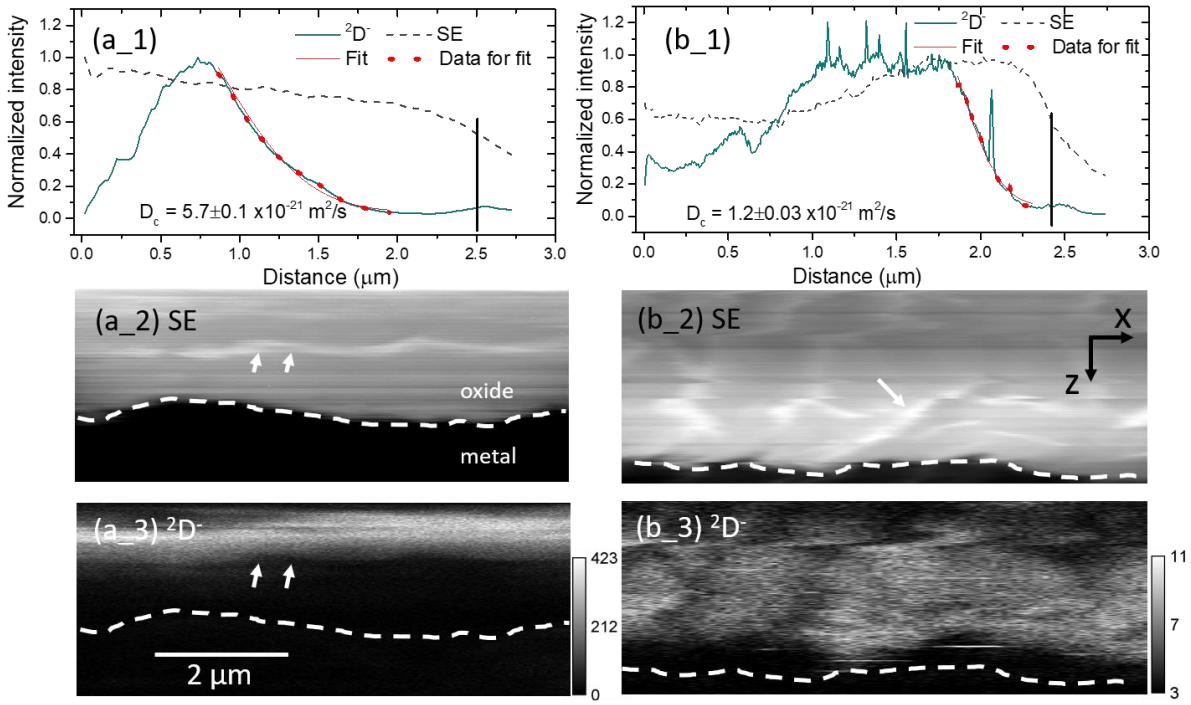

Figure 7. Depth profile and cross-sectional views of 3D data from samples 2.5Nb-3 and 2.5Nb-4 in panels a_x and b_x, respectively. 1, 2 and 3 represent the depth profile plot, cross-section view of secondary ion image and the cross-sectional view of the secondary ion $^2D^-$ signal respectively, all extracted from the 3D data. The intensities of $^2D^-$ and secondary electron signals were normalised by the intensity at the surface (at 0 μm), and the vertical black lines on the depth profile and white dashed lines on the cross-sectional images mark the position of the metal/oxide interface. Fitting the diffusion coefficients of deuterium through the oxide was carried out using Fick's 2nd law on the sections of the depth profiles marked with dots. The white arrows in the SE and $^2D^-$ maps mark the original locations of the Nb-rich β-Zr phase.

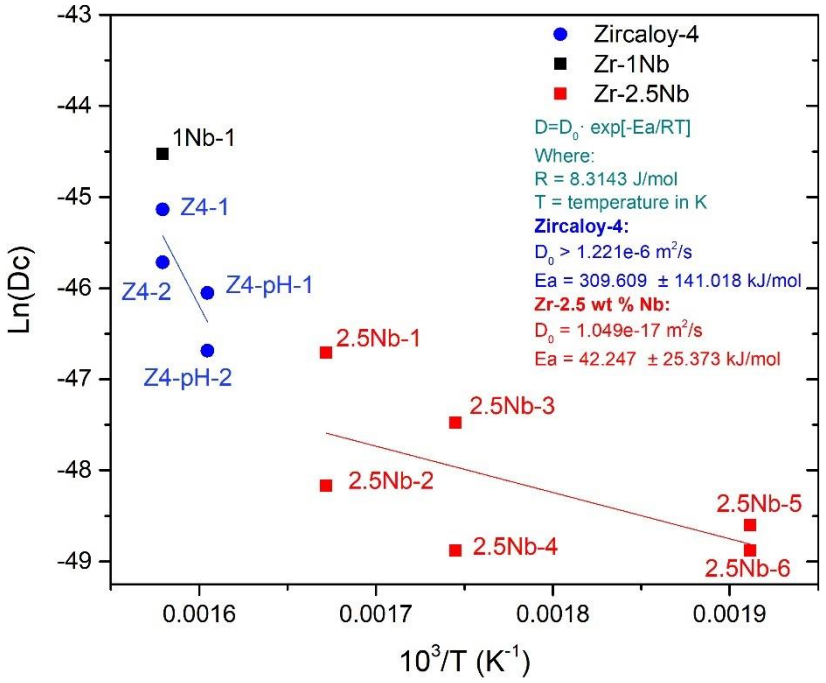

Figure 8. Arrhenius plot of deuterium diffusion in zirconium oxides on different alloys and estimated activation energies (Ea).

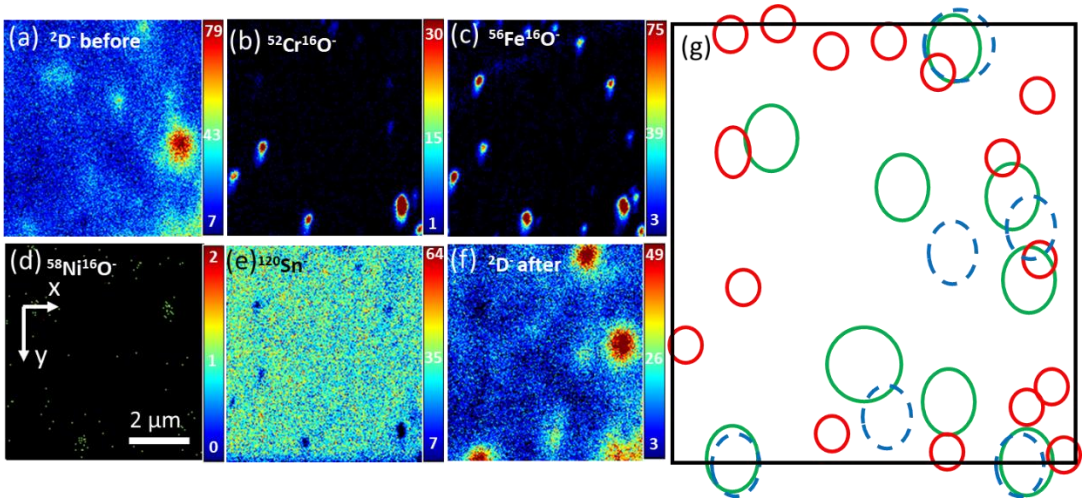

Figure 9. Results of experiments to correlate the locations of deuterium hot spots and SPPs in a Z4-2 sample. (a) and (f) are NanoSIMS maps identifying the locations of deuterium hot spots measured before and after retuning to locate SPPs. Images (b), (c), (d) and (e) are NanoSIMS maps of the $^{52}Cr^{16}O^{-}$, $^{56}Fe^{16}O^{-}$, $^{58}Ni^{16}O^{-}$ and $^{120}Sn^{-}$ secondary ion signals, respectively. Image (g) shows schematically the relative positions of deuterium hot spots and SPPs in this imaged area. Green solid circles and blue dashed circles are the deuterium hot spots measured respectively before and after SPP analysis. Red solid circles mark the locations of SPPs.

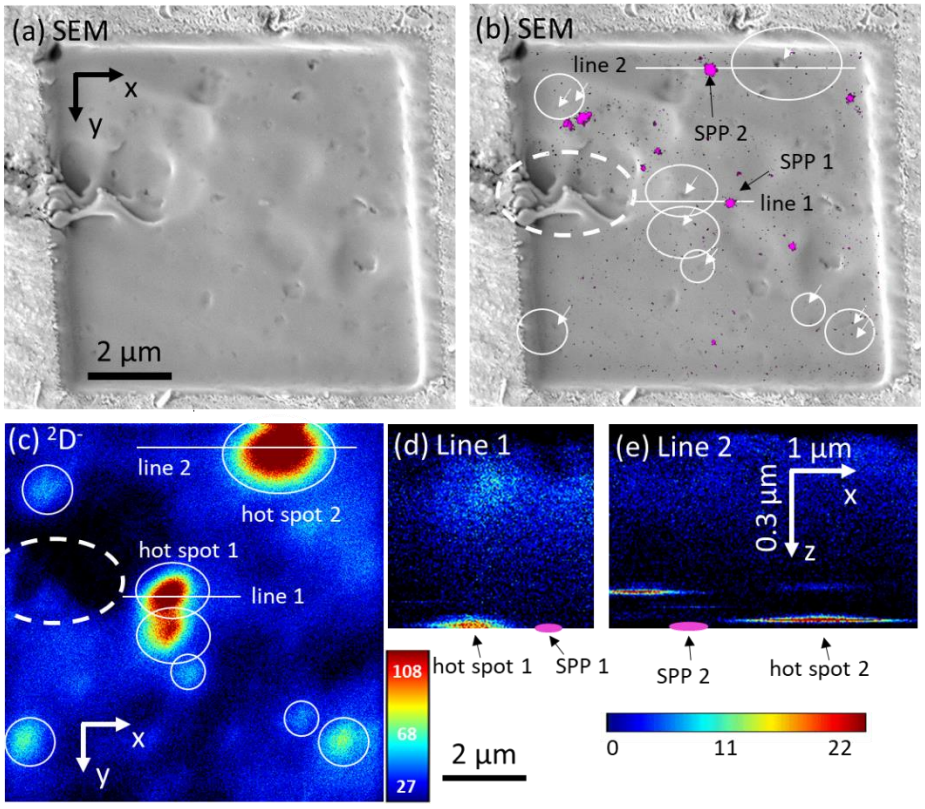

Figure 10. Results of experiments to correlate the locations of deuterium hot spots, cracks and iron-containing SPPs. Image (a) is the SEM image of a crater bottom in the middle of the oxide on sample Z4-1. Image (b) shows EDX maps of the positions of iron-containing SPPs (magenta spots) on the crater bottom. Small cracks are identified by white arrows and a large crack marked by a dashed circle. Image (c) is an accumulated $^{2}D^{-}$ ion image from the final 40 planes (~ 20 nm analysed thickness) before the EDX analysis. Image (d) and (e) are cross-section views (x-z) along lines 1 and 2 in image (b) showing the locations of both the $^{2}D^{-}$ hotspots and the iron-containing SPPs.

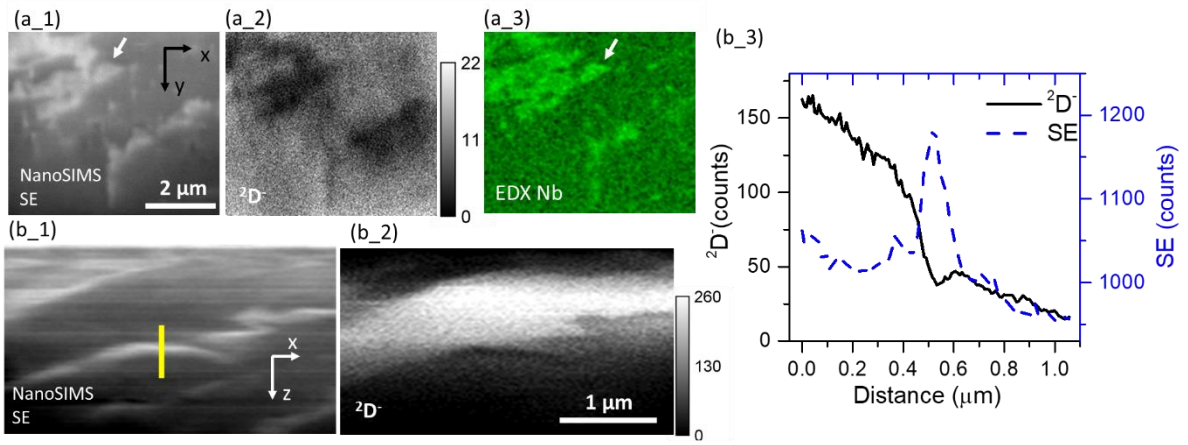

Figure 11. Correlating NanoSIMS secondary electron (SE) and $^2D^-$ signals from 2.5Nb-3 sample with the location of Nb-rich regions from the same surface. Image a_1 and a_2 are the NanoSIMS secondary electron (SE) image and the distribution of $^2D^-$, respectively, and a_3 the EDX Nb map. Images b_1 and b_2 are cross-sectional views of the 3D NanoSIMS data showing the SE image and the distribution of $^2D^-$ and b-3 shows the line scans for these signals along the line marked in b-2. White arrows in (a_1) and (a_3) mark the origianl locations of the Nb-rich β-Zr phase.

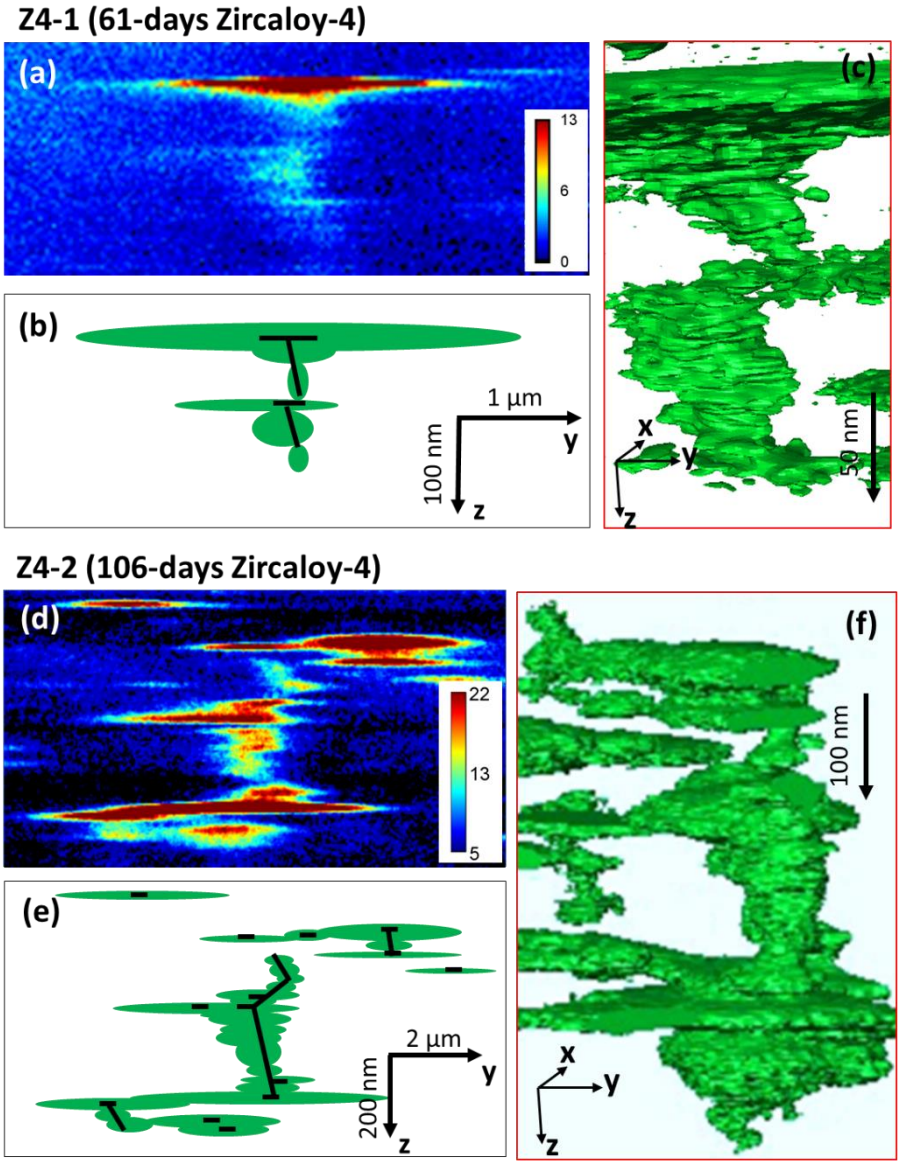

Figure 12. The hypothesis for the nature of the deuterium diffusion pathways. Image (a) and (d) are cross-section deuterium secondary ion image from sample Z4-1 and Z4-2, respectively. Image (b) and (e) are schematic shows the deuterium trapped regions in green and potential cracks or interconnected porosity in the oxide in black. Image (c) and (f) are the 3D views. Images (c) and (f) are 3D views reprinted from Figure 9 of [39], Copyright (2019), with permission from Elsevier.

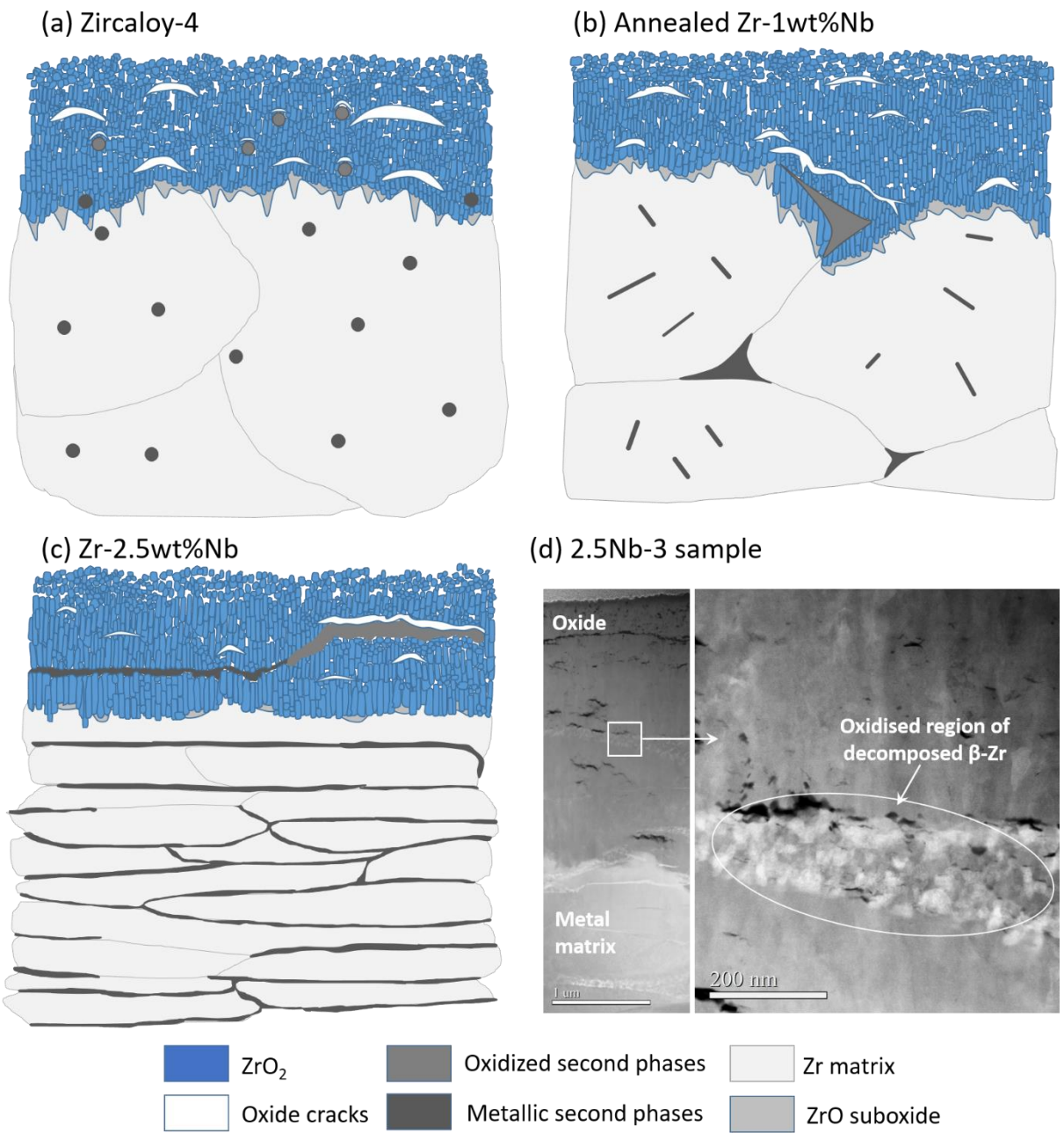

Figure 13. Schematic representations of the microstructures of the oxides and metal matrix of 3 types of corroded zirconium alloys in (a), (b) and (c), (d) is STEM HAADF images showing the complex mixture of phases formed by oxidation of the decomposed β-Zr phase in a Zr-2.5Nb alloy.

.